

Effect of Inductive Coil Geometry on the Operating Characteristics of a Pulsed Inductive Plasma Accelerator

Ashley Kristin Hallock

A DISSERTATION
PRESENTED TO THE FACULTY
OF PRINCETON UNIVERSITY
IN CANDIDACY FOR THE DEGREE
OF DOCTOR OF PHILOSOPHY

RECOMMENDED FOR ACCEPTANCE
BY THE DEPARTMENT OF
MECHANICAL AND AEROSPACE ENGINEERING

Advisors: Professor Richard B. Miles, Professor N. Jeremy Kasdin

June 2012

UMI Number: 3522411

All rights reserved

INFORMATION TO ALL USERS

The quality of this reproduction is dependent on the quality of the copy submitted.

In the unlikely event that the author did not send a complete manuscript and there are missing pages, these will be noted. Also, if material had to be removed, a note will indicate the deletion.



UMI 3522411

Copyright 2012 by ProQuest LLC.

All rights reserved. This edition of the work is protected against unauthorized copying under Title 17, United States Code.



ProQuest LLC.
789 East Eisenhower Parkway
P.O. Box 1346
Ann Arbor, MI 48106 - 1346

© Copyright by Ashley Kristin Hallock, 2012. All rights reserved.

Abstract

The effect of inductive coil geometry on the operating characteristics of a pulsed inductive plasma thruster is investigated analytically and experimentally. Coil inductance is measured as a function of the position of a simulated current sheet and modeled using finite element analysis to develop a two-dimensional semi-empirical inductance relation that is used to expand a circuit-based acceleration model from one to two dimensions. The model includes electromagnetic and gas-dynamic forces but excludes any process to translate radial plasma motion into axial motion. Furthermore a magnetically-impermeable current sheet encompassing all the propellant for a pulse is assumed to form immediately at the start of the pulse and at the surface of the inductive coil. The two-dimensional acceleration model is nondimensionalized, yielding a set of dimensionless performance scaling parameters. Model results indicate that the introduction of radial current sheet motion caused by a conical inductive coil geometry (versus a flat circular plate) increases the axial dynamic impedance parameter at which thrust efficiency is maximized and generally decreases the overall achievable thrust efficiency. Operational characteristics of two thrusters with inductive coils of different cone angles are explored through thrust stand measurements and time-integrated, unfiltered photography. Trends in impulse bit measurements indicate that, in the present configuration, the thruster with the inductive coil possessing a smaller cone angle produced larger values of thrust, in apparent contradiction to results of the model. Areas of increased light intensity in photographs of thruster operation are assumed to qualitatively represent locations of increased current density. Light intensity is generally greater in images of the thruster with the smaller cone angle when compared to those of the thruster with the larger half cone angle for the same operating conditions, and generally decreases in both thrusters for decreasing mass flow rate and capacitor voltage. The location of brightest light intensity shifts upstream for decreasing mass flow rate of propellant and downstream for decreasing applied voltage. Recognizing that there exists an optimum ratio of applied electric field to pressure with respect to breakdown efficiency, this result may indicate that the optimum ratio was not achieved uniformly over the coil face, leading to non-uniform, weak current sheet formation in violation of the model assumption of immediate formation from all injected propellant of a magnetically-impermeable current sheet.

Acknowledgments

(In order of appearance)

My parents, Terry and Charlie (and Mr. Bob), thank you for raising me with a love of science, math and engineering, and for giving me the freedom to make my own decisions. My sister, Stephanie, thank you for your support and for always having a place for me to sleep. My Aunt Cathy, thank you for buttons, and all the messages.

Professor Jahn, thank you for always making time to discuss my work, for reassuring me that the frustrations of experimental work are universal, and for encouraging me to never give up. Your mastery of many fields was always apparent in the well founded advice you generously offered.

Professor Miles and Professor Kasdin, thank you for your help in my transition to another lab, for your support, advice, encouragement, and for your patience.

Professor Cohen, Professor Efthimion, and Professor Majeski, thank you for your time, your guidance, and your advice.

The amazing former and present students of Princeton University, Andrea Kodys, Slava Spektor, Jack Berkery, James Cooley, Luke Uribarri, Peter Norgaard, Danny Lev, Ben Journs, and Justin Little, thank you for all the various forms of help you have offered, often at times when your own deadlines were fast-approaching. Thank you Luke for showing me through example what it takes to properly investigate a problem, and efficiently acquire free food.

Thank you Danny for your friendship, for giving me a refreshing perspective on everything, for your much-appreciated humor, for staying late in the lab with me, and for grilling food (at all hours of the day and night) and me (in preparation for the General Exams).

Guido Parissenti, thank you for your friendship, for your humor, for teaching me about linux, and for the fruit.

Kurt Polzin, thank you for offering me the use of your lab, your equipment, and your time. Thank you for all of the paperwork, phone calls, meetings, and training you went through so that I could continue working on my project. Everything in this dissertation was only possible because of your generosity, your enthusiasm for contributing to the field, your patience, and your advice.

Gregory Emsellem, thank you for your friendship, for taking time I know you did not have to help me prepare for the General Exams, for introducing me to Starbucks (and duck), for teaching me what it truly takes to accomplish the difficult goals for which we strive, and

also for encouraging me to never give up.

Dave Kirtley and Anthony Pancotti, thank you for your time, your humor, and your advice (of all kinds).

The wonderful people of NASA Marshall Space Flight Center, Tommy Reid, Doug Galloway, Jessica Wood, Boise Pearson, Jim Martin, Adam Martin, Richard Eskridge, Bill Emrich, Noah Rhys, Adam Kimberlin, Omar Mireles, Tom Godfroy, Dave Bradley, thank you all for helping me in so many different ways. Thank you Jessica for your honesty, thoughtfulness, and determination. Thank you Noah for making me laugh, for your understanding, and for never making fun of the consumption of tofu. Thank you Boise, Adam M. and Richard for all of the white-board discussions. Thank you Jim for your contagious enthusiasm for experimental research and your patience. Thank you Adam K. for all of the support, technical and otherwise, that you provided to not only my project but almost every other project in the building. Thank you for juggling your responsibilities to find time to help me, you are the unsung hero of ER-24.

Michael LaPointe, thank you for your support (of all kinds), your encouragement, your humor, and your advice.

The interns, Ryan Sullenberger, Kevin Bonds, Valerie Hanson, Lindsay Walker, Brian Miller (potatoes!), Andrea Wong, Alex Toftul, Mark Becnel, Jarred Reneau, Jake Adwar, and Kevin Perdue, thank you all for your friendship, your fearlessness, and your invaluable help. Thank you Sully for making me laugh, and for the continue button. Thank you Kevin B. for all your help, for driving us to the cape, for teaching me to drive a stick shift, and for making me tiki lamps (I mean copper frusta). Thank you Alex for the strength and passion with which you apply yourself to your work and your life, for staying late in the lab with me, and for Bohemian Rhapsody. Thank you Kevin P. for your time, for making things that worked and worked well (and making them quickly), for never asking me for a drawing, for staying late in the lab with me, and for making me laugh.

This dissertation carries the designation T-3252 in the records of the Department of Mechanical and Aerospace Engineering. Support for the research was provided by the Princeton Program in Plasma Science and Technology, the Advanced In-Space Propulsion Program managed by Dr. Michael Lapointe, and the Office of the Chief Technologist In-Space Propulsion Program managed by Mr. Timothy Smith.

List of Symbols

\mathbf{B}	magnetic field (T)
C	capacitance (F)
\mathbf{E}	electric field (V/m)
E	energy (J)
F_i	force in the i -th direction (N)
I_1	coil current (A)
I_2	plasma current (A)
I_{sp}	specific Impuse (s)
I_{bit}	impulse bit (N-s)
\mathbf{j}	current density (A/m ²)
k	Boltzmann's constant $\left(\frac{\text{m}^2\text{kg}}{\text{s}^2\text{K}}\right)$
ΔL	change in total circuit inductance (H)
L_0	initial inductance (H)
L_C	coil inductance (H)
l_{coil}	coil length (m)
\mathcal{M}	local Mach number
M	mutual inductance (H)
$m(z)$	total propellant mass in current sheet (kg)
m_0	initial mass of current sheet (kg)
m_{bit}	mass of current sheet slug (kg)
m_i	mass of an ion (kg)
\dot{m}	mass flow rate (mg/s)
N	fit parameter

P_1	upstream pressure (Pa)
P_2	downstream pressure (Pa)
\bar{r}	averaged radial location (m)
Δr	radial displacement (m)
$\overline{r_{coil}}$	averaged coil radial location (m)
R_e	resistance in the driving circuit (Ω)
R_{coil}	inductive coil major radius (m)
r_{coil}	inductive coil minor radius (m)
R_{cs}	current sheet major radius (m)
r_{cs}	minor radius of current sheet frustum (m)
T_1	temperature of gas upstream of shock (K)
U	potential energy (J)
u	shock velocity (m/s)
\mathbb{V}	volume (m^3)
V	time-changing voltage on the capacitor (V)
V_0	initial voltage on the capacitor (V)
v_r	radial velocity (m/s)
v_z	axial velocity (m/s)
z	axial current sheet displacement (m)
z_0	axial decoupling length (m)
α	axial dynamic impedance parameter
η_t	thrust efficiency
γ	ratio of specific heats
λ	gas-dynamic force parameter
ϕ	radial dynamic impedance parameter
ψ_1, ψ_2	critical resistance ratios
$\rho_A(z)$	linear mass density distribution (kg/m)
θ	half cone angle (degrees)
Ξ	gas-dynamic pressure parameter

List of Figures

1.1	Pulsed inductive plasma thrusters [1, 2, 3] operate on propellant injected onto the face of a coil through which a high frequency current pulse creates an electromagnetic field that electrodelessly ionizes and accelerates the propellant.	3
1.2	A drawing [12] of the FARAD Proof-of-concept experiment. Propellant is ionized by a radio-frequency antenna upstream of a planar inductive coil and diffuses along applied magnetic field lines to a region of electromagnetic interaction with the coil.	6
1.3	A schematic [3] and photograph of the downstream injection scheme of the original pulsed inductive thruster.	8
2.1	Schematic of setup for controlled copper frustum displacement from the inductive coil.	11
2.2	Coils and copper conic frusta used in the experiment with labels corresponding to the entries in Table 2.1.	12
2.3	Copper trace design used to create the conical inductive coil. The top layer is shown in red, the bottom layer in blue, and where they are superposed in purple.	13

2.4	Experimentally measured total inductance for various inductive coil geometries as a function of current sheet displacement with a typical error bar shown. Pinched current sheet trajectories are represented as x's and unpinched current sheets are represented as circles.	15
2.5	Plot of nondimensionalized inductance L^\diamond vs. nondimensionalized current sheet displacement.	17
2.6	Finite element calculation results of nondimensionalized inductance as a function of nondimensionalized radial location at $z=0$	19
2.7	Experimentally-obtained inductance profiles for simulated compressed ("pinched") current sheets as a function of axial displacement with typical error bars shown and the corresponding values of $L_{tot}(r = 25\text{mm}, z)$ calculated using Eq. (2.8).	20
2.8	Finite element results of inductance as a function of radial compression of current sheets at two different axial displacements in four different coil geometries. The corresponding function $L_{tot}(r, z)$ (Eq. (2.8)) is shown as a set of solid lines.	21
2.9	Results of finite element magnetic field calculations for a varying simulated current sheet axial displacement from the coil. The coil and simulated current sheet are labeled in the middle left panel and the coordinates are labeled in the upper left.	22
2.10	Diagram of the inductive coil geometry.	23
2.11	Finite element results (represented by markers) and the semi-empirical model (represented by a red line) for the inductance as a function of average current sheet radial position. Coil geometry is designated in the lower-left corner of the plot.	23

2.12	Finite element results (represented by markers) and Eq. (2.8) (represented by a red line) for the inductance as a function of average current sheet radial position. Coil geometry is designated in the lower-left corner of the plot. . .	24
2.13	Finite element results (represented by markers) and Eq. (2.8) (represented by a red line) for the inductance as a function of average current sheet radial position. Coil geometry is designated in the lower-left corner of the plot. . .	24
2.14	Comparison between the functional form of fits for the inductance as a function of current sheet axial location. Exponential fits are shown in red and error function fits are shown in blue.	25
2.15	Comparison of the accuracy of two functional fits for the inductance as a function of current sheet axial and radial locations. Exponential fits are shown in red and error function fits are shown in blue.	26
3.1	Lumped element circuit model of a pulsed inductive thruster inductively coupled to a plasma.	28
3.2	Equivalent circuit of a pulsed inductive thruster inductively coupled to a plasma used to derive a set of governing equations to model thruster performance.	28
3.3	Current sheet velocities versus time where current sheets for longer inductive coils (20L and 38) have a more gradual acceleration that lasts longer relative to shorter inductive coils (12 and 20S).	31
3.4	Results of axial plasma acceleration modeling for different inductive coil geometries with un-pinched current sheets represented by solid lines and pinched current sheets represented by dashed lines.	32
3.5	Coils with a larger half cone angle experience a smaller loss of volume in which magnetic field is shielded during a current pulse.	33

3.6	Experimental data of simulated compressed current sheets and the corresponding values of $L_{tot}(r, z)$	37
4.1	Calculated thrust efficiency as a function of α for different radial current sheet displacements.	44
4.2	Model results of thrust efficiency as a function of ϕ for the unconstrained case with $\alpha = 0.6$	45
4.3	Contour plot of thrust efficiency as a function of α and ϕ	46
5.1	VAHPER thrust stand, image from Ref. [4].	49
5.2	Photograph of the thrust stand calibration setup[5].	50
5.3	Photographs of the inductive coil taken <i>Left</i> : from the top and <i>right</i> : along the thrust axis.	51
5.4	Photographs of <i>Left</i> : the downstream electrodes with a cover removed and <i>Right</i> : both electrodes with the cover attached.	52
5.5	Unfiltered 16 second exposure of the preionized proellant at $\dot{m} = 150$ mg/s.	53
5.6	Photograph of the capacitor bank and mechanical switch.	54
5.7	Thruster mounted on the thrust stand.	55
6.1	Typical capacitor bank discharge voltage and circuit current as a function of time with representative error bars shown.	57
6.2	Voltage measurements at the capacitor bank and at the thruster terminals during discharge for $V_0 = 100$ V with representative error bars shown.	57
6.3	Signal from the force transducer and its time integral.	58
6.4	<i>left</i> : An LGDT signal resulting from an applied impulse and <i>Right</i> : a comparison of the signal to a fitted damped sinusoidal waveform for $t > 0$	59
6.5	A plot of I_{bit} versus momentum imparted to the thrust stand by the solenoid.	59

6.6	Thrust arm displacement measurements for thruster 20L and thruster 38 for V_0 5 kV and $\dot{m} = 120$ mg/s with typical error bars shown.	60
6.7	Curve fitting results thrust arm displacement measurements for thruster 20L and thruster 38 for for $t > 0$, V_0 5 kV, and $\dot{m} = 120$ mg/s.	60
6.8	I_{bit} for thruster 20L as a function of \dot{m} with $V_0 = 5$ kV.	61
6.9	Base pressure in the vacuum vessel as a function of \dot{m}	62
6.10	Time-integrated photographs of thruster 20L operating on 120 mg/s with <i>Top Left</i> : $V_0 = 5$ kV, <i>Top Right</i> : $V_0 = 4$ kV, and <i>Bottom</i> : $V_0 = 3$ kV.	63
6.11	Time-integrated photographs of thruster 20L operating on (from left to right, top to bottom) 150, 90, 30, 18, 15, and 12 mg/s with $V_0 = 5$ kV.	64
6.12	Time-integrated photographs of thruster 38 operating on <i>Top Left</i> : 120 mg/s, <i>Top Right</i> : 90 mg/s, and <i>Bottom</i> : 45 mg/s with $V_0 = 5$ kV.	65
6.13	Time-integrated photographs of thruster 20L and 38 operating on <i>Top</i> : 120 mg/s and <i>Bottom</i> : 90 mg/s with $V_0 = 5$ kV. Photographs were obtained at the same zoom level and camera orientation with respect to each thruster. . .	66

List of Tables

2.1	Notational reference labels and parameters for each of the inductive coil geometries studied.	13
2.2	Notational reference labels and parameters for each of the current sheet geometries studied.	14
2.3	Fit parameters for various unpinched current sheet geometries.	14
2.4	Increase in parasitic inductance values arising from the use of initially pinched current sheet geometries.	16
3.1	Final exhaust velocities for various current sheet geometries.	33
3.2	Final exhaust velocities for various current sheet geometries.	38
3.3	Minimum loss of kinetic energy due to radial current sheet compression. . .	39

Contents

Abstract	iii
Acknowledgments	iv
List of Symbols	vi
List of Figures	vii
List of Tables	xiii
1 Introduction	1
1.1 Advantages of Pulsed Plasma Acceleration	1
1.2 Pulsed Inductive Plasma Thrusters	2
1.3 Previous Work	4
1.3.1 The Pulsed Inductive Thruster	4
1.3.2 Faraday Accelerator with Radio-frequency Assisted Discharge	5
1.4 Motivation: Propellant Utilization Inefficiency	7
1.4.1 Inductive Coil Geometry	7
1.5 Dissertation Outline	9
2 Experiment for Measuring Coil Inductance as a Function of Simulated Current Sheet Dynamics	10
2.1 Experimental Setup	11
2.2 Experimental Results	13
2.3 Analysis of Experimental Results	14

2.4	Development of a Two-dimensional Semi-empirical Inductance Relation . .	17
2.4.1	A Purely Radial Semi-empirical Inductance Relation	18
2.4.2	Two-dimensional Semi-empirical Inductance Relation	19
2.4.3	Numerical Validation of the Two-dimensional Inductance Relation .	20
3	Pulsed Inductive Acceleration Modeling	27
3.1	One-dimensional Lumped Element Circuit Model	27
3.2	Application of the One-dimensional Model to Conical Geometries	30
3.2.1	One-dimensional Model Results and Analysis	31
3.3	Expansion of the Model to Two Dimensions	34
3.3.1	Incorporation of the Two-dimensional Semi-empirical Inductance Relation	34
3.3.2	An Estimate of the Gas-dynamic Pressure	35
3.4	Results	37
4	Model Analysis	40
4.1	Nondimensional Solution Approach	40
4.2	Nondimensional Scaling Parameters	41
4.3	Effect of Radial Motion on Thrust Efficiency	43
4.4	Summary of Results	46
5	Experiment for Measuring Thruster Operating Characteristics	48
5.1	Vacuum Facility	48
5.2	Thrust Stand	48
5.3	The Thruster	50
5.3.1	Inductive Coil	50
5.3.2	Preionization and Propellant Injection	51
5.3.3	High Power Switch and Capacitor Bank	53

5.4	Experimental Setup	54
6	Measurements and Analysis of Thruster Operating Characteristics	56
6.1	Capacitor Bank Voltage and Driving Current	56
6.2	Impulse Calculations	57
6.2.1	Effective Mass Calculation: Thrust Stand Calibration	58
6.2.2	Thrust Arm Displacement Measurements	60
6.2.3	Impulse Calculation	61
6.3	Photographic Evidence	62
7	Summary and Conclusions	68
7.1	Summary of Analytical Modeling Results	68
7.2	Summary of Experimental Results	71
7.3	Comparison of Experimental and Analytical Results	73
	Bibliography	75

Chapter 1

Introduction

IT is desirable to extend the lifetime and increase the reliability of an in-space propulsion system as much as possible since hardware maintenance or replacement becomes particularly challenging once a spacecraft has been placed into orbit. In addition, the amount of payload as a percentage of the total vehicle mass can be increased if the size and mass of the propulsion system, including the propellant required to complete a mission, can be reduced. The high values of specific impulse associated with electric propulsion (EP) generally allow for a reduction in the amount of propellant needed for a given mission as compared to conventional chemical propulsion systems.

1.1 Advantages of Pulsed Plasma Acceleration

In general, plasma thruster efficiency increases with increasing processed power since the energy cost associated with propellant ionization decreases as a fraction of total power. This applies to all thrusters that employ electromagnetic fields to drive current in the ionized propellant. Electric propulsion schemes achieve high values of specific impulse using applied electrostatic or electromagnetic body forces to accelerate propellant to a high velocity relative to that achievable through thermal gas expansion. While available power in

space is presently limited to tens of kilowatts, pulsed thrusters offer the capability of operating at higher power levels. These thrusters have operated successfully at 60-70 Joules per pulse in space, and up to 4 kJ per pulse in laboratory testing, and offer the potential to process very high levels of power using a single thruster by increasing the pulse rate[6].

Pulsed thrusters that operate by inductively driving current through propellant to produce electromagnetic body forces offer an increased lifetime over thrusters with electrodes where direct plasma-electrode interaction can lead to lifetime-limiting electrode erosion. In addition, the absence of any interaction between the propellant and metallic electrodes allows for operation of inductive pulsed plasma thrusters on a wider variety of propellants. They have been successfully operated on ammonia, hydrazine, and CO₂[2, 3], and there is no fundamental reason why they would not operate on *in situ* propellants like H₂O.

Pulsed inductive plasma thrusters are capable of maintaining constant per pulse specific impulse I_{sp} and thrust efficiency η_t over a wide range of input power levels by adjusting the pulse rate to maintain a constant discharge energy per unit pulse. It has also been demonstrated that a dynamically impedance-matched pulsed inductive plasma accelerator can operate in a regime where η_t is relatively constant over a wide range of I_{sp} values[2, 3].

1.2 Pulsed Inductive Plasma Thrusters

Pulsed inductive plasma thrusters [1, 2, 3] are spacecraft propulsion devices in which electrical energy is capacitively stored and then discharged through an inductive coil. An azimuthal time-varying current density \mathbf{j} is driven in the coil, producing a magnetic field \mathbf{B} in the manner described by Ampere's law:

$$\nabla \times \mathbf{B} = \mu_0 \mathbf{j} \quad (1.1)$$

where μ_0 is the magnetic permeability of free space. For an azimuthal \mathbf{j} , the magnetic field is produced with r - and z -components that permeate the volume surrounding the inductive coil. Since the current in the inductive coil is time varying, the magnetic field that it produces is as well, inducing an azimuthal electric field (\mathbf{E}) according to Faraday's law:

$$\nabla \times \mathbf{E} = -\partial \mathbf{B} / \partial t \quad (1.2)$$

This electric field, where sufficiently strong, causes propellant breakdown (ionization), producing a conducting plasma, and drives an azimuthal plasma current in the direction opposed to the initial current density \mathbf{j} , creating a magnetic field in opposition to the impinging field. The main thrust producing mechanism lies in the electromagnetic force exerted on the plasma emanating from the coil as the magnetic pressure increases between the inductive coil and the current ring in the propellant. Another equivalent way to view the acceleration mechanism is as a Lorentz body force arising from the interaction of the magnetic field and the induced current in the propellant. Through pulsed electromagnetic acceleration exhaust velocities as high as ($\mathcal{O}(10 - 100 \text{ km/s})$) have been achieved.

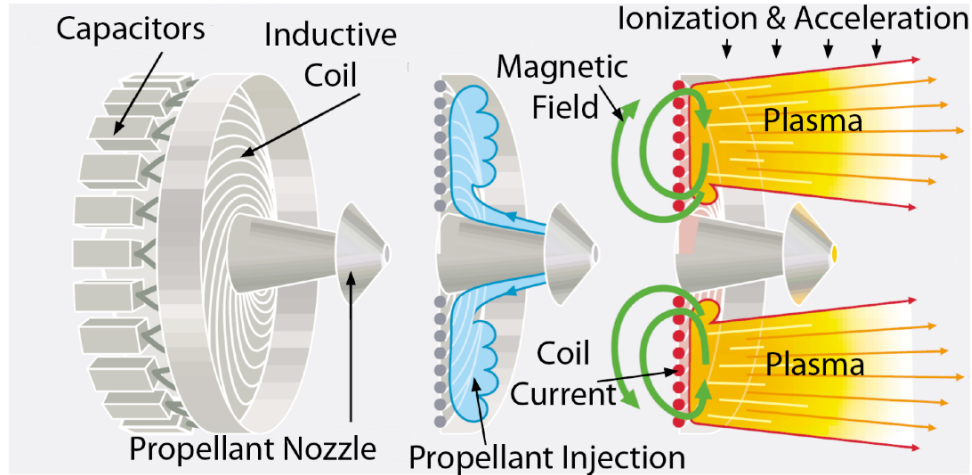


Figure 1.1: Pulsed inductive plasma thrusters [1, 2, 3] operate on propellant injected onto the face of a coil through which a high frequency current pulse creates an electromagnetic field that electrodelessly ionizes and accelerates the propellant.

The general configuration of an inductive plasma thruster is shown in Fig. 1.1. As in directly coupled pulsed plasma thrusters, the capacitors are attached as close as possible to the inductive coil to minimize stray inductance, maximizing the amount of voltage that is dropped across the driving coil as compared to that dropped across the rest of the circuit. Propellant injection is not restricted to using a downstream nozzle in the manner illustrated in Fig. 1.1, but this scheme has been shown to be successful[2, 7] despite the obvious disadvantage of the protruding structure interfering with the ejected plasma plume. Thrust efficiency of this type of device depends upon the ability to inductively ionize propellant and efficiently accelerate the induced current sheet axially away from the coil.

1.3 Previous Work

1.3.1 The Pulsed Inductive Thruster

The Pulsed Inductive Thruster (PIT) evolved from a conceptual accelerator to what is presently the state-of-the-art for pulsed inductive plasma accelerators during the time period from the mid 1960s to the early 1990s. This evolution was the result of research and development by the TRW Space Systems team in Redondo Beach, CA led by R.H. Lovberg and C.L. Dailey. The body of work resulting from the efforts of this group represents a majority of the knowledge base for this thruster class.

During this time, the basic current sheet acceleration mechanism was investigated with the conclusion that electrons represent the major current carriers as they are more mobile and easily driven azimuthally by the induced fields in the propellant, and that the ambipolar electric field created by their axial acceleration under the action of a Lorentz body force subsequently accelerates the trailing ions. A model was developed treating the electrical circuit as a collection of lumped elements. This model, coupled to a one-dimensional momentum equation, predicts approximately constant efficiency over a wide range of spe-

cific impulse with maximum efficiency coinciding with operating conditions where the timescale of current sheet motion is properly matched to the timescale of the driving circuit.

Large-scale thrusters (with diameters of 1 meter and operating at approximately 4 kJ/pulse) were constructed and showed promise as a competitive electric propulsion scheme during testing, exceeding 50% efficiency when operating on ammonia propellant. Experimental results on ammonia agreed favorably with results of the circuit model, specifically demonstrating constant thrust efficiency over a wide range of specific impulse. Many lessons were learned during testing, including the benefits of maximizing the initial driving current rise rate and the necessity of minimizing inductance in all thruster components except the inductive coil.

During early investigations [8], several smaller-scale thrusters were constructed for proof-of-concept experiments in which the effect of the driving circuit properties on thruster efficiency were investigated. The difficulties of propellant utilization efficiency were revealed by experiments where thrusters with a planar inductive coil placed in backfilled environments outperformed those employing discrete propellant injection.

1.3.2 Faraday Accelerator with Radio-frequency Assisted Discharge

Many technological challenges associated with the PIT stem from the high voltage required for inductive breakdown of neutral propellant. While preionization was explored during early investigations of a smaller-scale thruster at TRW, it was restricted to the use of an initial current pulse through the coil immediately preceding the main discharge, and was not thoroughly investigated. The underlying concept of partially ionizing propellant to permit better inductive energy transfer to the plasma during a subsequent main energy discharge is well known and has been repeatedly and successfully employed [9, 10, 11].

A proof of concept experiment at Princeton University, the Faraday Accelerator with

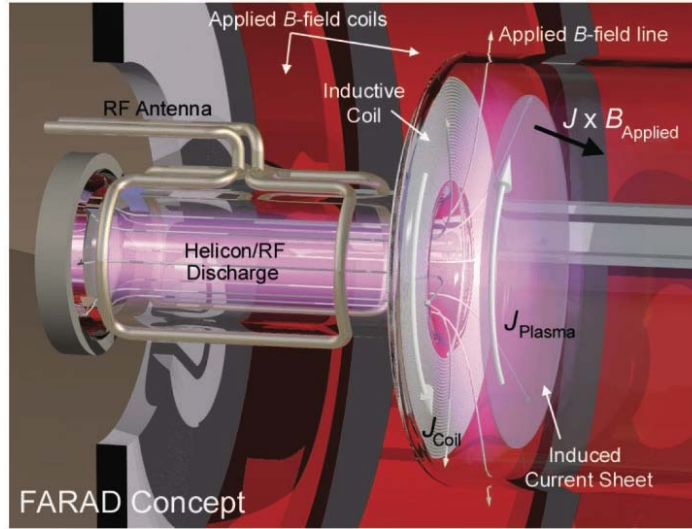


Figure 1.2: A drawing [12] of the FARAD Proof-of-concept experiment. Propellant is ionized by a radio-frequency antenna upstream of a planar inductive coil and diffuses along applied magnetic field lines to a region of electromagnetic interaction with the coil.

Radio-frequency Assisted Discharge [1, 12, 13] (FARAD), demonstrated the feasibility of using a radio-frequency ionization source in conjunction with a planar inductive coil to produce and accelerate a current sheet at discharge energies below 100 J/pulse, as compared to the 4 kJ/pulse previously employed by others in larger-scale devices. The ionization source of the FARAD experiment, shown in a drawing in Fig. 1.2, provided seed electrons that permitted further inductive ionization and acceleration by current pulsed through the inductive coil. In this setup a pulse energy $\mathcal{O}(100 \text{ J})$ at a charging voltage $\mathcal{O}(1 \text{ kV})$ was sufficient for current sheet creation and acceleration. For comparison, typical pulse energies for the PIT (with no preionization scheme employed) were $\mathcal{O}(1000 \text{ J})$ and charging voltages were on the order of $\mathcal{O}(10 \text{ kV})$. Current sheet formation was only achieved with the aid of an applied magnetic field that directed charged particles to the face of the coil, sufficiently increasing the density until inductive interaction was possible. The electromagnetic interaction weakens quickly with axial displacement, so directing the preionized plasma close to the coil face was critical in this experiment.

1.4 Motivation: Propellant Utilization Inefficiency

Ideally, when a current sheet is formed within the confines of the inductive coil, it perfectly shields the fields produced by the coil such that the inductance presented to the driving circuit by the inductive coil is initially low, growing as the plasma accelerates away from the coil. According to the Lovberg criterion, the achievable electromagnetic acceleration efficiency in a pulsed device is largely governed by the inductance of the coil and how its inductance changes as the current sheet accelerates. The limit on electrical efficiency η_t is given as

$$\eta_t \leq \frac{\Delta L}{L_0} \quad (1.3)$$

where ΔL is the change in total circuit inductance as the plasma moves, and L_0 is any stray circuit inductance.

1.4.1 Inductive Coil Geometry

Work on pulsed inductive thrusters from the 1960s through the 1990s focused on a flat inductive coil where the outer diameter was varied, but the angle between the surface of the coil and the horizontal remained 90° . The coil is directly facing space, and as such a downstream propellant injection scheme, shown in Fig. 1.3, was required to provide sufficient propellant density at the coil face for plasma production and subsequent acceleration.

Jahn [14] has stated that:

“Once a breakdown is established, it must intensify rapidly to a current layer that is stable, that covers the entire channel cross section, that is of sufficiently high conductivity to make resistive losses negligible, and that is sufficiently dense to be impermeable to the ambient gas which it must accelerate. These requirements bear, first, on the characteristics of the external circuit, which must deliver sufficient total current at sufficiently rapid rise time that the skin effect operates effectively at the

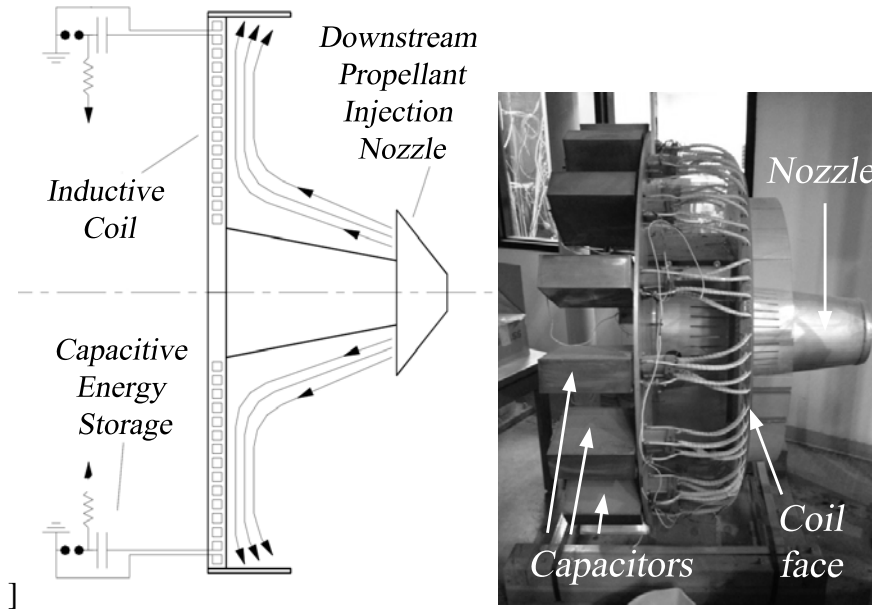


Figure 1.3: A schematic [3] and photograph of the downstream injection scheme of the original pulsed inductive thruster.

attainable gas conductivity; second, on the ambient gas density, which must be high enough to sustain the arc, but not so high as to overload it with excessive mass; and third, on the channel geometry, which must lend itself to a transverse current zone across the entire section.”

The second and third points of the second sentence emphasize that the thruster must deliver to and keep propellant at the coil face until the discharge begins without obstructing the progress of the subsequent current sheet as it is accelerated away from the inductive coil towards the vacuum of space. One proposed solution is to alter the coil geometry such that it more closely follows the natural diffusive path of the injected propellant from inlet to vacuum. A cone or cylinder can be envisioned to provide more gas containment than a flat plate. The work presented in this dissertation explores how modifying the inductive coil to a conical geometry would affect the performance of an inductive plasma thruster.

1.5 Dissertation Outline

This dissertation describes an investigation of the effect of inductive coil geometry on the performance of an inductive plasma thruster. Specifically, it explores the effect of transitioning from the flat-plate coil to a conical coil geometry. An experiment to model the ideal change in coil inductance as a function of current sheet position for multiple coil geometries is described in Chapter 2 along with a comparison of the resulting experimental data to results from magnetic field modeling and simulations. The expansion of a one-dimensional thruster performance model to two dimensions is described in Chapter 3, followed by nondimensionalization and analysis of the model in Chapter 4. Material from Chapters 2 - 4 can be found in References [15], [16], and [17]. An experiment to evaluate the performance of two thrusters of differing inductive coil geometry is described in Chapter 5 while the results and discussion appear in Chapter 6. Conclusions are presented in Chapter 7.

Chapter 2

Experiment for Measuring Coil Inductance as a Function of Simulated Current Sheet Dynamics

THE change in inductance presented to the electrical circuit as the plasma is accelerated away from the coil is the primary factor governing the electromagnetic acceleration process as it represents the electromagnetic work that can be performed on the plasma. A semi-empirical formula for this relation has been developed for purely axial current sheet locations, and has been successfully used in conjunction with a circuit-based acceleration model to predict thruster performance [2]. Expansion of this relationship to two-dimensions would allow the modeling of two-dimensional current sheet motion. This chapter describes an experiment to determine this relationship for two-dimensional current sheet motion in various inductive coil geometries.

2.1 Experimental Setup

To measure the inductance as a function of current sheet position, we constructed inductive coils of various geometries and measured the total inductance of these coils as a function of the displacement of a copper frustum that simulates the presence of a current sheet. We assume that the current sheet geometry will mirror the coil geometry that formed it (*i.e.* maintain the same cone angle for all time). Two simulated current sheets were constructed for each coil geometry. One frustum fit tightly against the inner surface of the coil while the second has a different minor radius r_{cs} to simulate radial compression (or pinching) of the current sheet. Pinching motion is assumed to leave the half cone angle θ unchanged and the frustum length equal to l_{coil} , which is defined as:

$$l_{coil} = (R_{coil} - r_{coil}) / \tan(\theta).$$

where r_{coil} is the minor radius of the coil and R_{coil} is the major radius.

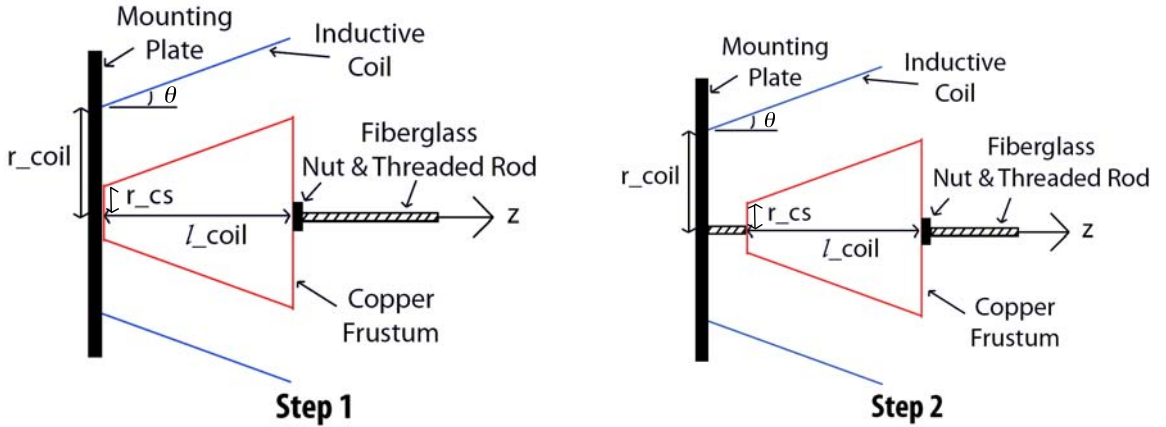


Figure 2.1: Schematic of setup for controlled copper frustum displacement from the inductive coil.

Copper frusta were constructed from flat copper sheets whose thickness of 1.6 mm (0.062 in) exceeds five skin depths and ideally shields 99.9% of the energy of an impinging electromagnetic field. The copper frusta were electrically isolated and fitted with insulating

conic sections that held a fiberglass nut on the centerline. A schematic of the experimental setup to control axial translation of the frusta is shown in Fig. 2.1 and a photograph of the inductive coils and their associated copper frusta are shown in Fig. 2.2.

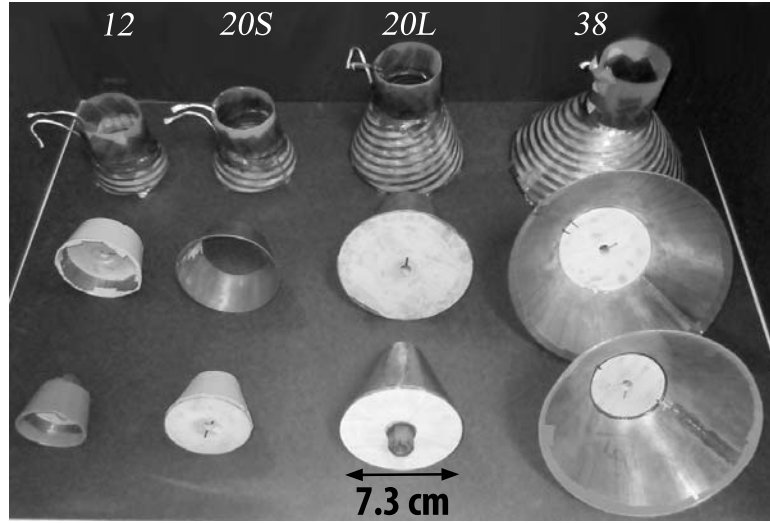


Figure 2.2: Coils and copper conic frusta used in the experiment with labels corresponding to the entries in Table 2.1.

The inductive coils were constructed from 0.2 mm (0.008 in) thick copper strips and 0.05 mm (0.02 in) thick mylar. The pattern of the copper traces, shown in Fig. 2.3, is such that the radial and axial components of current from the two sides of the mylar will cancel, yielding a uniform, azimuthal current at the coil face (as in the PIT [2]). Current is fed to each trace individually via coaxial cables connected in parallel at the upstream end, or smaller end, of the cone. Each current trace follows an Archimedes spiral, completing two full turns while traveling along the entire axial length of the frustum twice before the path returns to the point of origin on the opposite side of the mylar insulation.

Four different inductive coil geometries (varying in l_{coil} and/or θ) were studied, and for each inductive coil geometry two current sheet geometries (varying in minor and major radius) were studied representing two different levels of current sheet “pinching”. These geometries are described in Tables 2.1 & 2.2 (the “P” at the end of those references associated with radially compressed current sheet geometries stands for “pinched”, the “S”

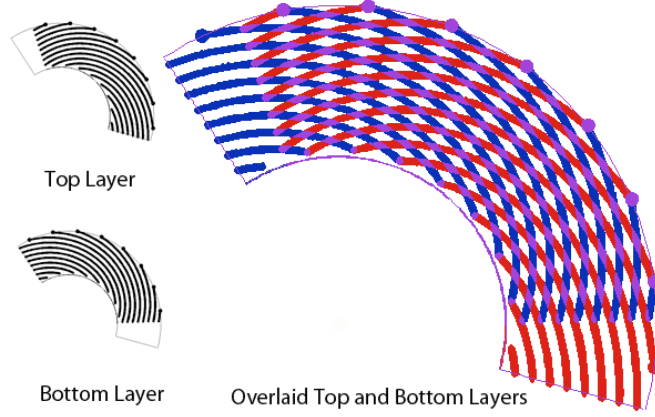


Figure 2.3: Copper trace design used to create the conical inductive coil. The top layer is shown in red, the bottom layer in blue, and where they are superposed in purple.

reference	θ (degrees)	l_{coil} (cm)	r_{coil} (cm)
12	12	4.3	4
20S	20	5	4
20L	20	10	4
38	38	10	4

Table 2.1: Notational reference labels and parameters for each of the inductive coil geometries studied.

stands for “short”, and the “L” stands for “long”).

2.2 Experimental Results

The total inductance (L_{tot}) was measured at 84 axial locations using an Agilent 4285A precision LCR meter. The data for each coil/“current sheet” combination are shown in Fig. 2.4 as a function of axial copper frustum displacement. We calculate values of L_0 , L_C , and z_0 for each coil geometry by fitting these data to an expression for the inductance as a function of current sheet axial position, given as:

$$L_{tot}(z) = L_0 + L_C (1 - \exp(-z/z_0)), \quad (2.1)$$

where L_{tot} is the total inductance in the thruster, L_0 is the inductance everywhere in the

reference	θ (degrees)	l_{coil} (cm)	r_{cs} (cm)
CS12	12	4.3	3.9
CS12P	12	4.3	2.5
CS20S	20	5	3.9
CS20SP	20	5	2.5
CS20L	20	10	3.9
CS20LP	20	10	2.5
CS38	38	10	3.9
CS38P	38	10	2.5

Table 2.2: Notational reference labels and parameters for each of the current sheet geometries studied.

Current Sheet	L_C (nH)	z_0 (cm)
CS12	564	2.6
CS20S	624	2.6
CS20L	450	4.0
CS38	558	3.6

Table 2.3: Fit parameters for various unpinched current sheet geometries.

driving circuit except the coil, and z_0 is the axial decoupling distance. From this empirically determined function it is clear that L_C is the maximum amount by which L_{tot} can be changed as a result of changing current sheet position, and we refer to it as the accessible inductance. This accessible inductance represents the potential energy available for conversion to axial current sheet velocity. Eq. (2.1) has been used with success to fit the axial inductance profiles in flat coil (90°) accelerators[2, 3]. Values for L_C and z_0 found by curve fitting the data for the four different coil geometries and unpinched frusta studied are shown in Table 2.3 .

2.3 Analysis of Experimental Results

The coil with the lowest accessible inductance (L_C), 20L, is taken as a baseline to which the other geometries can be compared. In attempting to maintain the same number of turns for all coils, the pitch angle of the traces in coils with a smaller l_{coil} was decreased such that the azimuthal component of the current in the traces was increased. Since the radial

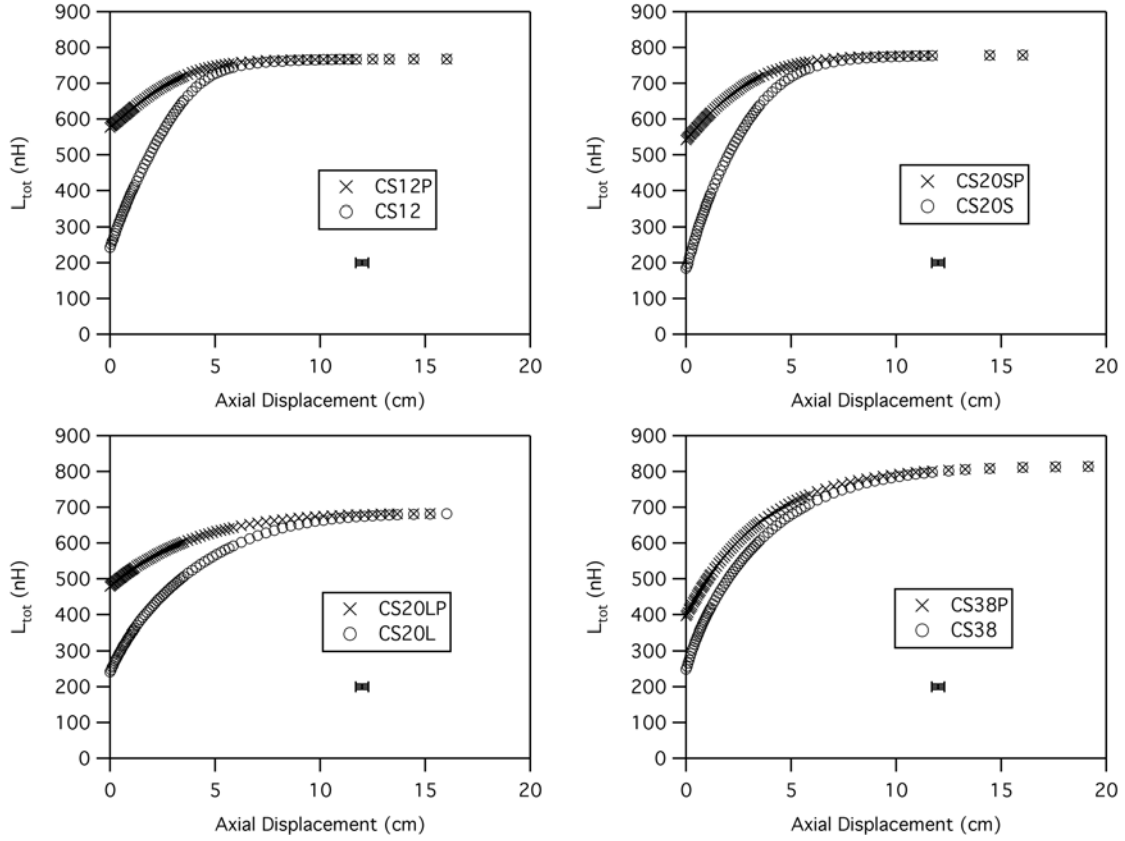


Figure 2.4: Experimentally measured total inductance for various inductive coil geometries as a function of current sheet displacement with a typical error bar shown. Pinched current sheet trajectories are represented as x's and unpinched current sheets are represented as circles.

and axial current components in the coil cancel (on average) by design, the field arising from the azimuthal coil current is stronger for a given applied current in the shorter coil, contributing to a higher coil inductance.

The loss of accessible inductance incurred by the pinched current sheets relative to the unpinched current sheets, designated by ΔL_0 and shown in Table 2.4, was calculated by taking the difference between L_C (or the value of L_{tot} at $z = 0$) for the pinched and unpinched current sheets. This additional inductance can be seen in Fig. 2.4 as a higher value for inductance at $z = 0$ for the pinched current sheets. From these data we conclude that pinched current sheets show weaker initial coupling to the inductive coil.

Nondimensionalization of Eq. (2.1) by L_C to produce a general relation for the change

Current Sheet	L_0 (nH)	ΔL_0	z_0 (cm)
CS12P	445	333	2.6
CS20SP	466	357	2.6
CS20LP	344	238	4.0
CS38P	247	147	3.6

Table 2.4: Increase in parasitic inductance values arising from the use of initially pinched current sheet geometries.

in total measured inductance as a function of current sheet axial position yields the following expression:

$$L_{tot}/L_C = L_0/L_C + (1 - \exp(-z/z_0)) \quad (2.2)$$

The first term on the right hand side of Eq. (2.2) represents a constant parasitic inductance inaccessible for current sheet acceleration. The second term represents the total accessible inductance potentially convertible to current sheet acceleration. It is this second term that isolates the effect of coil geometry on current sheet acceleration, and we label this value L^\diamond :

$$L^\diamond = \frac{L_{tot} - L_0}{L_C} = 1 - \exp(-z/z_0) \quad (2.3)$$

To isolate the effect of coil geometry from the influence of the driving circuit, we calculated L^\diamond for each axial location by subtracting the value of L_0 from each data point and non-dimensionalizing to L_C . The results are shown in Fig. 2.5 along with a plot of Eq. (2.3) (shown in red). Though none of the coil geometries studied had an angle close to the 90° of the PIT MkV coil, the data were still in relatively good agreement with Eq. (2.3).

The similarity of the nondimensionalized inductance measurements for each geometry suggests that for any given current sheet geometry within the range of parameters studied here, values for the accessible inductance of the driving coil, L_C , and the decoupling distance z_0 can be determined using Eq. (2.1). The fact that all data collapse when nor-

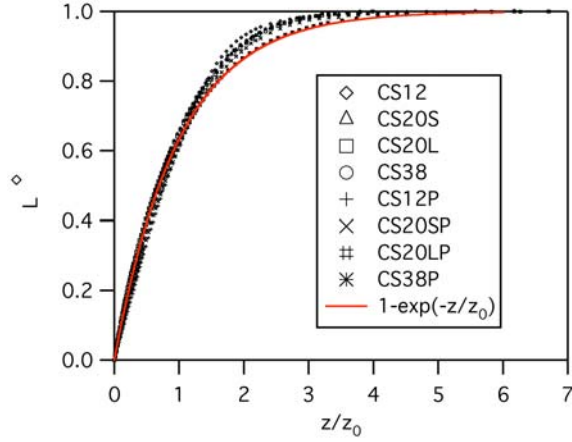


Figure 2.5: Plot of nondimensionalized inductance L^\diamond vs. nondimensionalized current sheet displacement.

malized indicates that the accessible inductance percentage decrease relative to L_C as the current sheet displaces axially from the driving coil is the same for all four coil geometries. The accessible inductance for both pinched and unpinched current sheets decreases in the same sense qualitatively as a percentage of the initial value (value at $z = 0$) as the current sheet decouples from the coil, even though current sheet pinching causes a decrease in the initial accessible inductance (or increase in the initial parasitic inductance). This decrease in accessible inductance for the pinched case can be thought of as the increase in initial inductance that would arise if the current sheet formed at the decreased (pinched) radial location instead of forming at the coil face and then pinching/translating to that location.

2.4 Development of a Two-dimensional Semi-empirical Inductance Relation

The experimental data presented in this chapter are aimed at permitting the modeling of two-dimensional current sheet motion for calculation of thruster performance. The first step in this modeling is to develop a two-dimensional form of the inductance profile given in Eq. (2.1). We begin by developing an inductance relation that fits the data for pure radial

motion (current sheet at a constant axial location), and then combine the radial and axial descriptions to produce a two-dimensional relationship.

2.4.1 A Purely Radial Semi-empirical Inductance Relation

The variation in inductance data at $z = 0$ as a function of radial current sheet position is fit well by the function

$$L_{tot}(\bar{r}) = L_0 + L_C \left(1 - \left(\frac{\bar{r}}{\overline{r_{coil}}} \right)^N \right) \quad (2.4)$$

where \bar{r} is the average radial position of the current sheet

$$\bar{r} = \frac{(R_{cs} - \Delta r) + (r_{cs} - \Delta r)}{2}, \quad (2.5)$$

where R_{cs} is the current sheet major radius, r_{cs} is the current sheet minor radius, and Δr is the radial displacement from the coil minor and major radius, respectively, $\overline{r_{coil}}$ is the average radial location of the coil

$$\overline{r_{coil}} = \frac{R_{coil} + r_{coil}}{2}, \quad (2.6)$$

and N is a fit parameter that depends on coil geometry.

A nondimensional expression analogous to that of Eq. (2.3) can be written for the radial direction :

$$L^\# = 1 - (\bar{r}/\overline{r_{coil}})^N. \quad (2.7)$$

Eq. (2.7) is shown in Fig. 2.6 along with nondimensionalized inductance profiles at $z = 0$ that were calculated using a magnetostatic finite element analysis solver (described in detail in Section 2.4.3). The non-dimensionalized radial inductance relation for all geometries studied here collapse relatively well, giving some confidence in the fit function employed

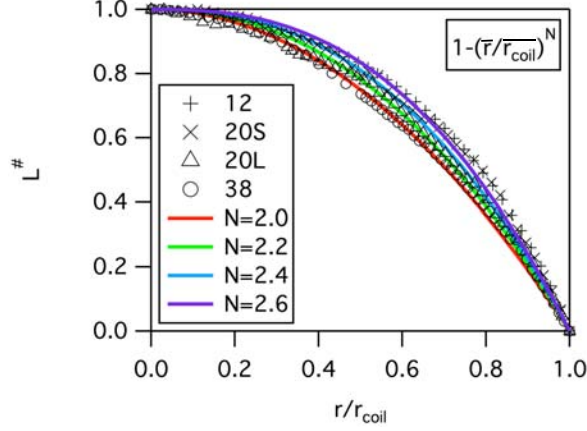


Figure 2.6: Finite element calculation results of nondimensionalized inductance as a function of nondimensionalized radial location at $z=0$.

(Eq. (2.7)).

2.4.2 Two-dimensional Semi-empirical Inductance Relation

Eq. (2.4) is combined with Eq. (2.1) in the following manner to yield a function for the two dimensional inductance variation:

$$L_{tot}(r, z) = L_0 + L_C \left(1 - \exp(-z/z_0) \left(\frac{\bar{r}}{r_{coil}} \right)^N \right) \quad (2.8)$$

Eq. (2.8) is shown in Fig. 2.7 along side experimental data of the coil inductance as a function of simulated pinched current sheet axial displacement. A comparison of Eq. (2.8) with calculated and experimental data show the difference to be well within the error bars.

The exponent N is found by fitting Eq. (2.8) to calculations of inductance as a function of radial current sheet compression at zero axial displacement obtained using finite element analysis (described in detail in the following section) to create a sufficiently large set for a fit. The results, shown in Fig. 2.8 as square markers, were fit in each case to Eq. (2.8) to find N . Also plotted in the figure is Eq. (2.8) for $z = 0$ and 5 cm and calculations using finite element analysis of inductance at an axial displacement of 5 cm (shown as cross markers).

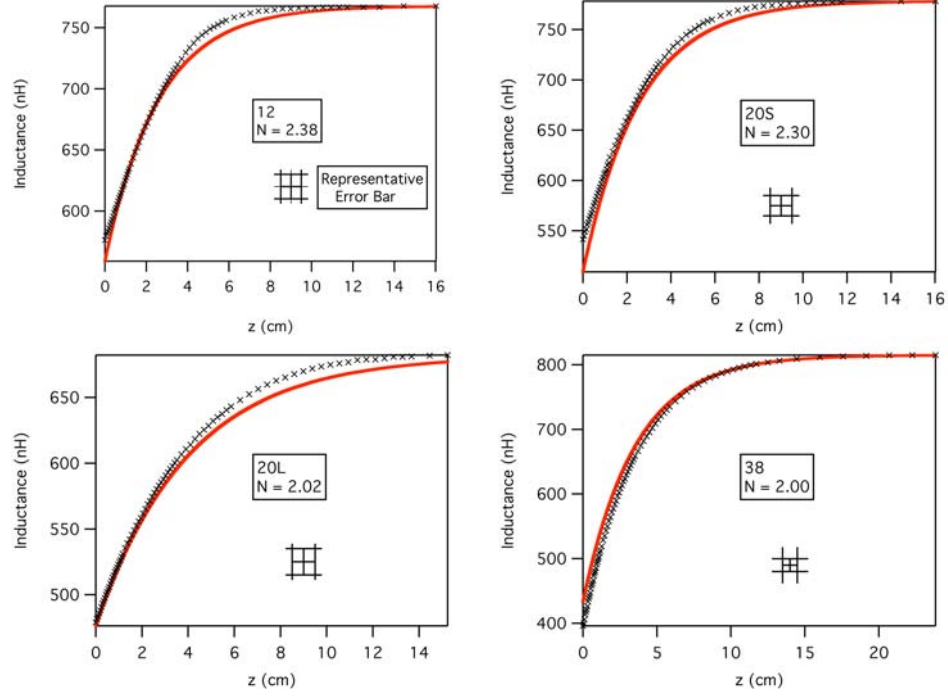


Figure 2.7: Experimentally-obtained inductance profiles for simulated compressed (“pinched”) current sheets as a function of axial displacement with typical error bars shown and the corresponding values of $L_{tot}(r = 25\text{mm}, z)$ calculated using Eq. (2.8).

2.4.3 Numerical Validation of the Two-dimensional Inductance Relation

Inductance as a function of two-dimensional current sheet position was calculated for various coil geometries with the use of a two-dimensional axisymmetric magnetostatic solver (QuickField, Tera Analysis, Los Angeles, CA) following the method described in Reference [18]. The program formulates the problem as the Poisson’s equation for vector magnetic potential \mathbf{A} ($\mathbf{B} = \nabla \times \mathbf{A}$) with either Dirichlet (used here) or Neumann boundary conditions. The Poisson’s equation is solved over an unstructured mesh through the successive over relaxation method, with convergence occurring when the change in field energy between iterations is below a certain threshold. The program uses automatic mesh refinement of the grid if the convergence threshold cannot be met.

The current sheet was modeled as an infinitely conductive conic frustum that mirrored

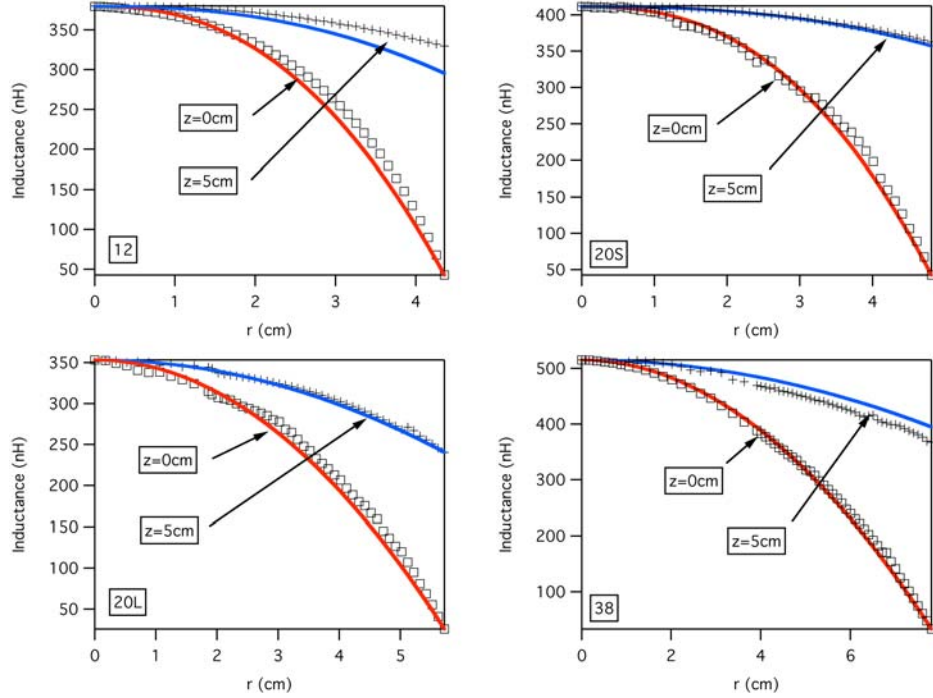


Figure 2.8: Finite element results of inductance as a function of radial compression of current sheets at two different axial displacements in four different coil geometries. The corresponding function $L_{tot}(r, z)$ (Eq. (2.8)) is shown as a set of solid lines.

the dimensions (length, cone angle) of the coil. A fixed current level was applied to the coil and the magnetic field produced by the coil-simulated current sheet system was calculated for different current sheet axial and radial positions. Results of magnetic field calculations are shown in Fig. 2.9 for various simulated current sheet axial locations. The field was integrated over the control volume (which extended sufficiently past the coil and current sheet to encompass a majority of the field energy) to calculate the total field energy, which was then multiplied by two and divided by the square of the input current to yield the total inductance of the configuration.

The coil geometry examined is shown and labeled in Fig. 2.10. The geometry is designated in the lower left hand corner of Figs. 2.11 - 2.13 where the number is the half cone angle θ and a suffix of “S”, “M” or “L” refers respectively to a short, 5 cm, medium 6-8 cm, or a long, 10 cm coil length l_{coil} . All coils had a minor radius r_{coil} of 4 cm, and the

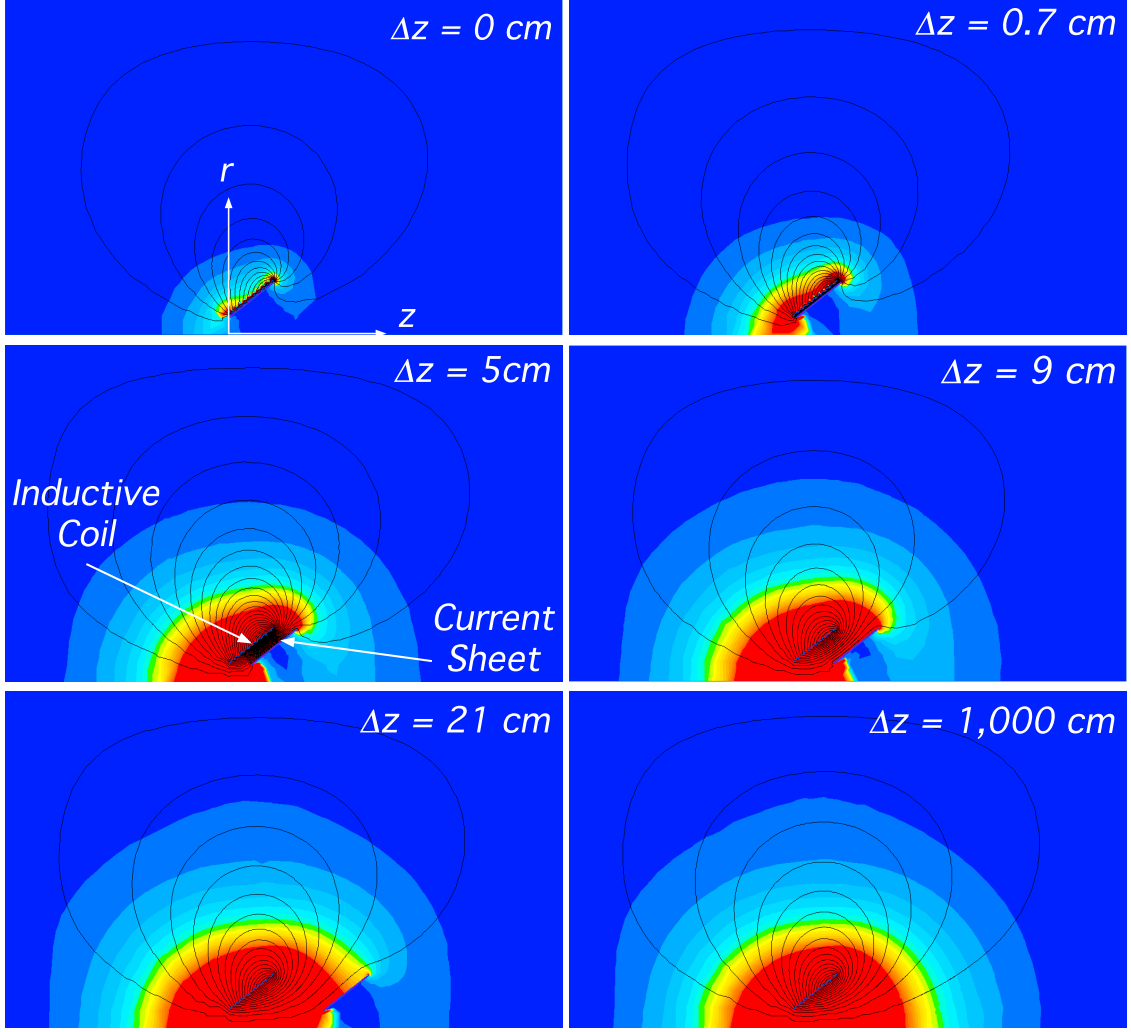


Figure 2.9: Results of finite element magnetic field calculations for a varying simulated current sheet axial displacement from the coil. The coil and simulated current sheet are labeled in the middle left panel and the coordinates are labeled in the upper left.

only coil with $l_{coil} = 0$ had a half cone angle of 90° (*i.e.* a flat plate coil).

The inductive coupling between coils and current sheets possessing geometries other than those of current sheets explicitly tested experimentally was explored through finite-element modeling to test the range of validity of Eq. (2.8). In each case, the coil inductance L_C and decoupling length z_0 were calculated by curve fitting Eq. (2.8) to the axial inductance profile found through modeling. This curve fit was performed for the inductance profile resulting from purely axial current sheet translation, or while holding $r = \overline{r_{coil}}$. The

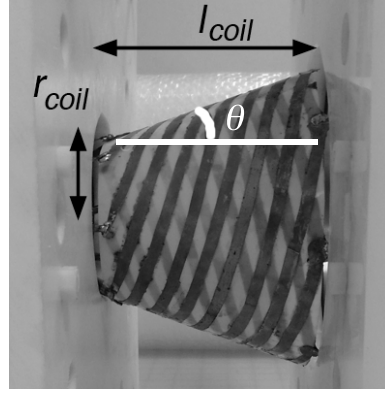


Figure 2.10: Diagram of the inductive coil geometry.

inductance was then calculated using finite element modeling for various current sheet radial and axial locations to produce the two-dimensional inductance profiles shown in Figs. 2.11, 2.12, and 2.13. Also shown are inductance calculations obtained using Eq. (2.8) with the fit parameters previously determined for data at $L_{tot}(0, z)$ and $L_{tot}(r, 0)$. The simulation data are plotted as markers and Eq. (2.8) is plotted as a red line. The finite element results and Eq. (2.8) show good quantitative agreement for half cone angles between 20° - 55° , as shown in Fig. 2.12, but this agreement begins to degrade outside this range, as shown in Figs. 2.11 and 2.13.

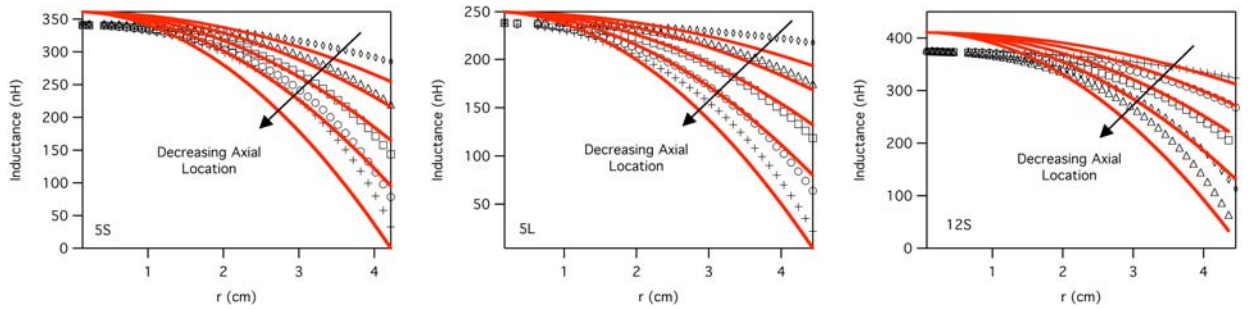


Figure 2.11: Finite element results (represented by markers) and the semi-empirical model (represented by a red line) for the inductance as a function of average current sheet radial position. Coil geometry is designated in the lower-left corner of the plot.

For coils with a half cone angle below 12° , it is the axial dependence of Eq. (2.8) that begins to fail to accurately represent finite element results. For these coil geometries the inductance as a function of axial current sheet location is fit more accurately by an error

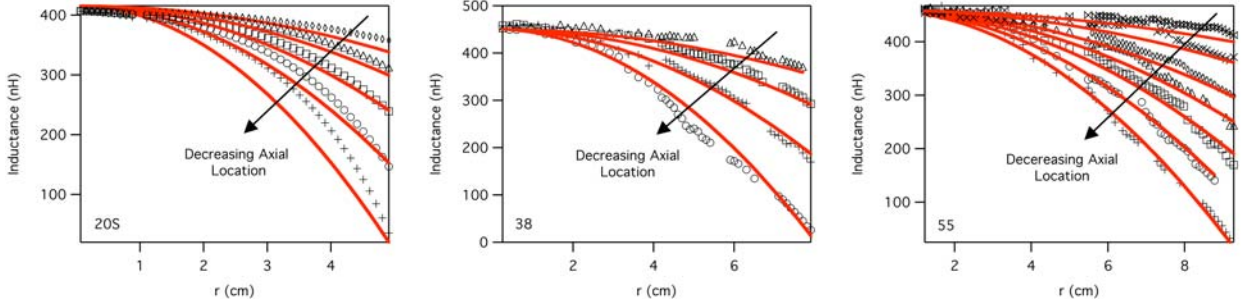


Figure 2.12: Finite element results (represented by markers) and Eq. (2.8) (represented by a red line) for the inductance as a function of average current sheet radial position. Coil geometry is designated in the lower-left corner of the plot.

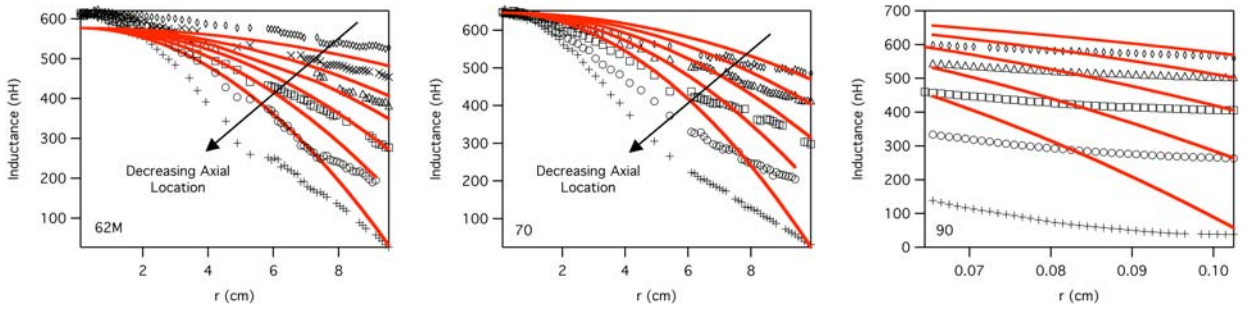


Figure 2.13: Finite element results (represented by markers) and Eq. (2.8) (represented by a red line) for the inductance as a function of average current sheet radial position. Coil geometry is designated in the lower-left corner of the plot.

function than an exponential, as shown in Fig. 2.14.

Plots of the inductance as calculated using the error function in place of the exponential in Eq. (2.8) are compared in Fig. 2.15 to inductance calculations using Eq. (2.8) for half cone angles of 0° and 5° . Below half cone angles of 12° , the accuracy with which inductance values calculated using the exponential function represent inductance values calculated using finite element analysis decreases with decreasing half cone angle, whereas for the error function this accuracy increases, as shown in Fig. 2.15.

For coils with a half cone angle above 55° , it is the radial dependence of Eq. (2.8) that begins to fail to accurately represent finite element results. While proposed functional forms for the radial dependence of coil inductance in this parameter space is outside the scope of this study, modeling results indicate that electromagnetic current sheet acceler-

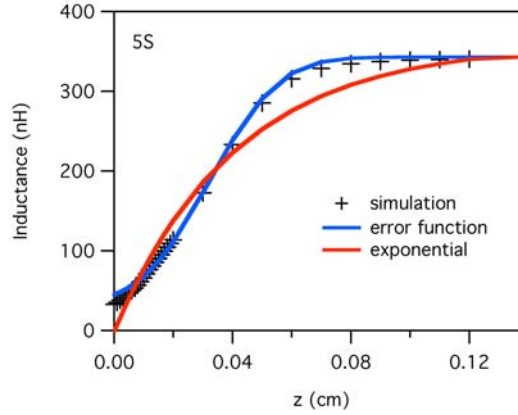


Figure 2.14: Comparison between the functional form of fits for the inductance as a function of current sheet axial location. Exponential fits are shown in red and error function fits are shown in blue.

ation in the radial direction decreases for increasing coil half cone angle, becoming negligible for half cone angles approaching 90° . Therefore the radial current sheet locations shown in Fig. 2.13 may not represent a physically realizable configuration. It is clear that two different functions are required to represent the radial dependence of the inductance of coils with cone angles approaching 0° and 90° , just as in the case of axial dependence. A global function that smoothly transitions between these different functional forms as the half cone angle varies from 0° to 90° would allow predictions over a wider parameter space of two-dimensional electromagnetic current sheet acceleration.

The utility of an analytic expression for the total thruster inductance as a function of two-dimensional current sheet position is demonstrated in the next Chapter where Eq. (2.8) is used to expand a one-dimensional thruster performance model to two dimensions.

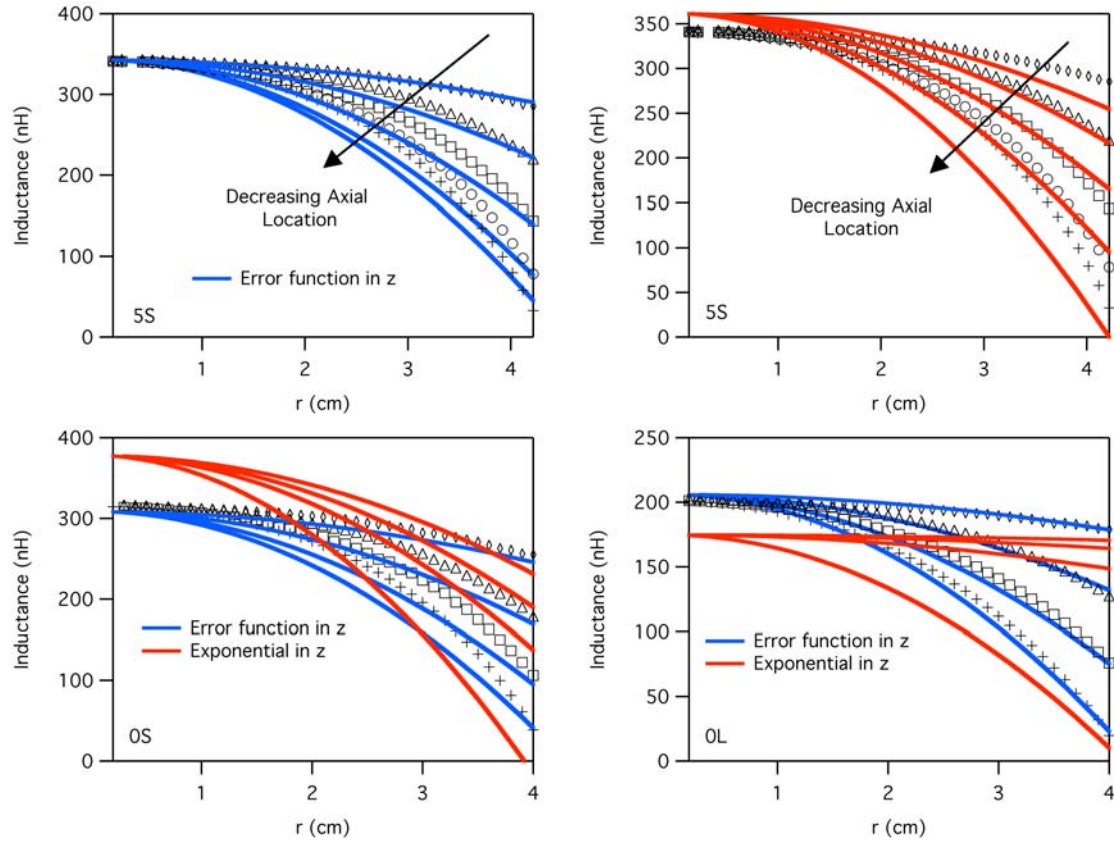


Figure 2.15: Comparison of the accuracy of two functional fits for the inductance as a function of current sheet axial and radial locations. Exponential fits are shown in red and error function fits are shown in blue.

Chapter 3

Pulsed Inductive Acceleration Modeling

A one-dimensional model of pulsed inductive current sheet acceleration is described and then expanded to two-dimensions with the use of the semi-empirical inductance relation developed in Chapter 2.

3.1 One-dimensional Lumped Element Circuit Model

Pulsed inductive thrusters are commonly studied with the use of the semi-empirical circuit model shown in Fig. 3.1. In the figure, I_1 is the current flowing in the driving circuit, I_2 is the current flowing in the plasma, C is the capacitance, M is the mutual inductance between the driving coil and the current sheet, L_0 is the initial (parasitic) inductance in the driving circuit, L_C is the coil inductance, R_p is the resistance of the plasma, and R_e is the resistance in the driving circuit.

An equivalent circuit can be drawn, shown in Fig. 3.2, from which a set of equations can be derived to model thruster performance. From this circuit diagram, where V_0 is the initial voltage on the capacitor and V is the voltage on the capacitor as a function of time, the following equations follow from the application of Kirchoff's law:

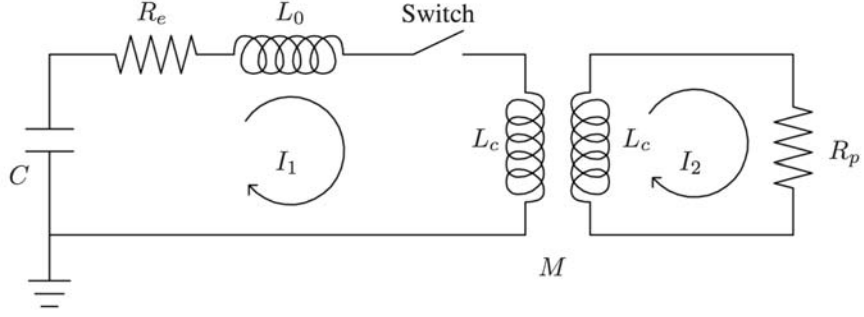


Figure 3.1: Lumped element circuit model of a pulsed inductive thruster inductively coupled to a plasma.

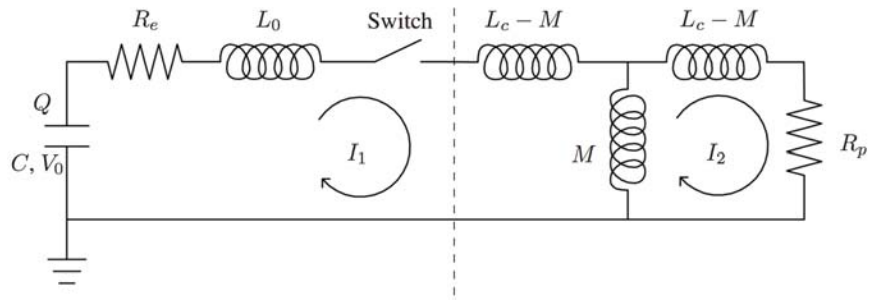


Figure 3.2: Equivalent circuit of a pulsed inductive thruster inductively coupled to a plasma used to derive a set of governing equations to model thruster performance.

$$\frac{dI_1}{dt} = \frac{L_C V - L_C R_e I_1 - M R_p I_2 + (L_C I_2 + M I_1) \frac{dM}{dt}}{L_C (L_0 + L_C) - M^2} \quad (3.1)$$

$$\frac{dI_2}{dt} = \frac{M \frac{dI_1}{dt} + I_1 \frac{dM}{dt} - R_p I_2}{L_C} \quad (3.2)$$

$$\frac{dV}{dt} = \frac{-I_1}{C} \quad (3.3)$$

The potential energy $U = LI^2/2$ of the inductive coil changes as a function of current sheet position, representing a force F_i on the current sheet equal along the direction of translation that can be written as [3]:

$$F_i = -\frac{\partial U}{\partial x_i} = \frac{I^2}{2} \frac{\partial L}{\partial x_i}. \quad (3.4)$$

The axial equation of motion for the current sheet can be written using Eq. (3.4) in Newton's second law and the snowplow model to describe how mass is accumulated by the current sheet:

$$\frac{dv_z}{dt} = \left[\frac{L_C I_1^2}{2z_0} \exp\left(-\frac{z}{z_0}\right) - \rho_A(z) v_z^2 \right] / m(z) \quad (3.5)$$

where z is the axial displacement of the current sheet from the driving coil, $m(z)$ is the total propellant mass in the current sheet, $\rho_A(z)$ is the linear mass density distribution, and v_z is the axial current sheet velocity

$$\frac{dz}{dt} = v_z. \quad (3.6)$$

In Eq. (3.5) the first term on the right hand side represents the electromagnetic force on the plasma, while the second term on the right hand side represents a drag force as the current sheet snowplows into neutral gas. The snowplow accumulated mass in the sheet is then given by

$$m(t) = \int_0^t \rho_A v_z dt' + m_0 \quad (3.7)$$

where m_0 is the initial mass in the current sheet. For the present study, the mass distribution was modeled as a slug ($\rho_A(z) = 0$, $m_0 = m_{bit}$) for simplicity.

Ignoring the resistive elements in Fig. 3.2, the lumped series and parallel inductive elements can be added to yield the total inductance,

$$L_{tot} = L_0 + L_C - \frac{M^2}{L_C}. \quad (3.8)$$

It can be seen from this equation that the total inductance changes as a function of time due to the time changing mutual inductance, which varies as the current sheet moves.

The well-known, semi-empirical inductance relation as a function of axial current sheet

position [2] introduced in Chapter 2,

$$L_{tot}(z) = L_0 + L_C (1 - \exp(-z/z_0)), \quad (3.9)$$

is used to determine an expression for the mutual inductance as a function of current sheet position. Eq. (3.9) can be set equal to the previous expression for total inductance (Eq. (3.8)) and solved for the mutual inductance as a function of the axial separation distance between the driving coil and the current sheet:

$$M = L_C \exp(-z/2z_0), \quad (3.10)$$

which has the time derivative

$$\frac{dM}{dt} = -\frac{L_C}{2z_0} \exp(-z/2z_0) \frac{dz}{dt}. \quad (3.11)$$

This closes the set of six coupled first-order ODEs, consisting of Eqs. (3.1), (3.2), (3.3), (3.5), (3.6), and (3.11), that can be readily solved numerically. Of these six governing equations only Eqs. (3.5) and (3.11) must be empirically found based upon the inductive coil geometry. While Eq. (3.9) and the subsequent derivation was developed for a planar coil geometry, it has been found to accurately represent the axial inductive coupling behavior of ring-shaped and conical coil geometries as well [19, 20].

3.2 Application of the One-dimensional Model to Conical Geometries

Values for L_0 , L_C and z_0 obtained in the experiment described in Chapter 2 were inserted into Eq. (2.1) to model thruster performance for each current sheet trajectory for each inductive coil geometry. A constant value of parasitic inductance of 100 nH is assumed

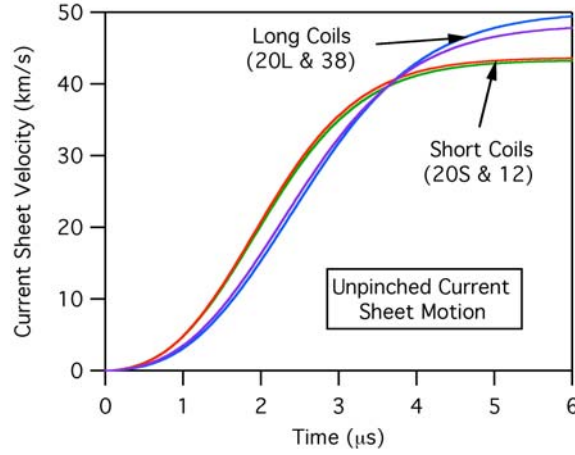


Figure 3.3: Current sheet velocities versus time where current sheets for longer inductive coils (20L and 38) have a more gradual acceleration that lasts longer relative to shorter inductive coils (12 and 20S).

for each case. For unpinched current sheets, this is equal to the total initial inductance of the circuit, while the additional parasitic inductance listed in Table 2.4 is added to the external inductance to yield a greater initial inductance for pinched current sheets. The model predicts the velocity of the current sheet as a function of time. These predictions are presented in Figs. 3.3 & 3.4, with the former isolating the effect of coil length l_{coil} and the latter focusing on the effects of the half cone angle θ and the minor radius of the simulated current sheet frustum r_{cs} where changes in r_{cs} simulate current sheet pinching.

3.2.1 One-dimensional Model Results and Analysis

The results plotted in Fig. 3.3 show that those axially translating current sheets created in the longer coil/current sheet combinations experience a less intense acceleration process over a longer time relative to the shorter coils, ultimately leading to a higher final exhaust velocity than in the shorter coil/current cases. This result implies that the inductance changes more rapidly for the short coils, but that the current sheet is electromagnetically coupled to the acceleration coil over a greater distance for the longer coils, leading to a higher exhaust velocity. The observed trend is preserved for the longer and shorter pinched

current sheets.

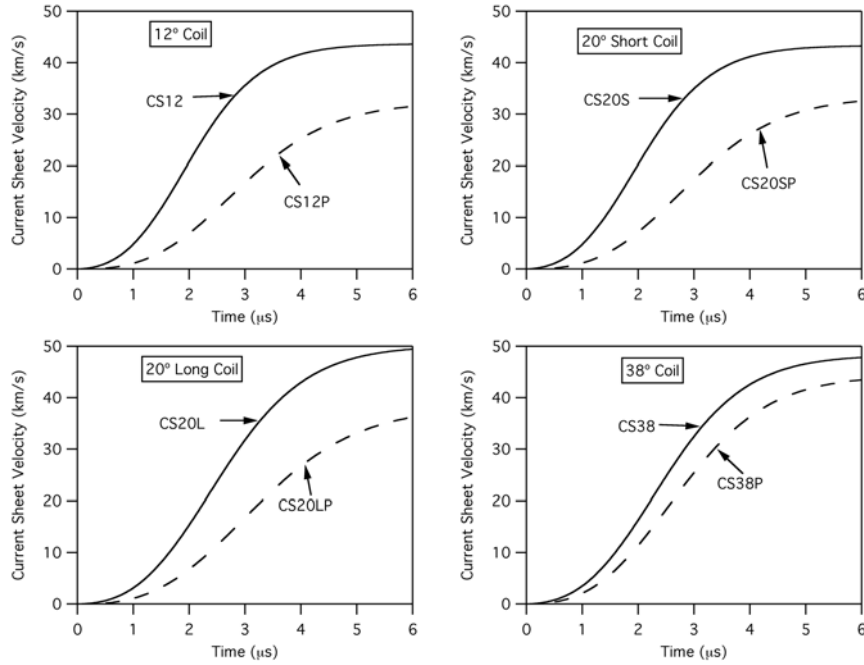


Figure 3.4: Results of axial plasma acceleration modeling for different inductive coil geometries with un-pinched current sheets represented by solid lines and pinched current sheets represented by dashed lines.

When comparing the model results for the velocity of unpinched and pinched current sheets in Fig. 3.4, it appears that when the current sheet is pinched it decouples from the driving coil faster. This implies a decrease in the achievable stroke length or, equivalently, an increase in the initial inductance presented to the driving circuit. Stated differently, the electromagnetic field energy available to axially accelerate the plasma is reduced for a current sheet that experiences more pinching. The final axial exhaust velocities attained by all current sheet geometries studied under pure electromagnetic forces with purely axial translation are shown in Table 3.1, along with the percentage loss of exhaust velocity and directed kinetic energy resulting from the sheet being pinched throughout its existence.

As the half cone angle of an inductive coil is increased the accelerator exhibits lower susceptibility to performance loss due to radial current sheet displacement. The explanation for this property lies in the change in volume available for a magnetic field to occupy in each

Unpinched Cases	v_z (km/s)	Pinched Cases	v_z (km/s)	velocity loss $\frac{\Delta v}{v_{zmax}}$	KE loss
CS12	44	CS12P	31	30 %	50%
CS20S	43	CS20SP	33	23 %	41%
CS20L	49	CS20LP	36	27 %	46%
CS38	48	CS38P	43	10 %	20%

Table 3.1: Final exhaust velocities for various current sheet geometries.

conical inductive coil/current sheet configuration relative to the initial available volume. For efficient thruster operation, the initial inductance presented to the circuit by the coil should be minimized. Stated another way, the initial volume occupied by the field generated by the coil should be minimized. This is accomplished when the current sheet forms as close to the driving coil as possible because the field from the current sheet and the coil are summed between the coil and the current sheet and mostly cancel everywhere except between the coil and current sheet. A radial displacement of the current sheet increases the available volume between coil and current sheet less for coils of larger θ . The decrease in the volume enclosed by the current sheet ΔV as a fraction of the initial volume enclosed by the current sheet V_0 is shown in Fig. 3.5 for the four coil geometries studied. This change in volume is representative of a loss of volume capable of shielding field generation at $z = z_0$.

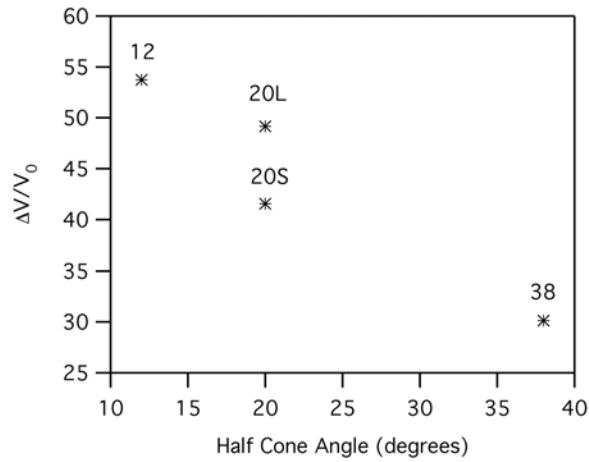


Figure 3.5: Coils with a larger half cone angle experience a smaller loss of volume in which magnetic field is shielded during a current pulse.

The model has previously only included the effects of axial electromagnetic current sheet acceleration, however in a conical geometry there will be axial as well as radial gradients in the inductance. The presence of a radial inductance gradient leads to a radial component of the Lorentz force on the current sheet, which will in turn compress the plasma and give rise to a gas-dynamic pressure force opposing the radial Lorentz force. To more accurately capture the underlying physical mechanisms of current sheet acceleration, the one dimensional expressions for electromagnetic forces described above are expanded to two dimensions in the following section. After this, a method to estimate the time-dependent gas-dynamic pressure on the propellant is presented.

3.3 Expansion of the Model to Two Dimensions

The goal of the development of the two-dimensional expression for inductance (presented as Eq. (2.8)) is to be able to predict its value at any point in the r - z domain knowing only L_C , z_0 , N and the coil radius, angle and length. While it is possible that there may be a relation encompassing all of these parameters that would obviate the need for experimental determination of the inductance profile, finding that solution is beyond the scope of the present work.

3.3.1 Incorporation of the Two-dimensional Semi-empirical Inductance Relation

The one-dimensional model presented above can be expanded to two dimensions by replacing Eq. (3.9) with the two-dimensional semi-empirical inductance relation of Eq. (2.8) that was developed and validated in Chapter 2,

$$L_{tot}(r, z) = L_0 + L_C \left(1 - \exp(-z/z_0) \left(\frac{\bar{r}}{r_{coil}} \right)^N \right). \quad (3.12)$$

This leads to a new form for Eq. (3.10),

$$M = L_C \exp(-z/2z_0) \left(\frac{\bar{r}}{r_{coil}} \right)^{N/2}. \quad (3.13)$$

The time derivative of M is then

$$\frac{dM}{dt} = \frac{L_C}{r_{coil}^N} \frac{N}{2} \bar{r}^{\frac{N}{2}-1} \frac{dr}{dt} \exp(-z/2z_0) - \frac{L_C}{2z_0} \exp(-z/2z_0) \frac{dz}{dt} \left(\frac{\bar{r}}{r_{coil}} \right)^{N/2}. \quad (3.14)$$

With a known two-dimensional functional dependence of inductance, a momentum equation can now be written for both the axial and radial directions:

$$\frac{dv_z}{dt} = \left[\frac{L_C I_1^2}{2z_0} \exp\left(-\frac{z}{z_0}\right) \left(\frac{\bar{r}}{r_{coil}} \right)^N \right] / m_{bit}, \quad (3.15)$$

$$\frac{dv_r}{dt} = \left[-\frac{L_C I_1^2 N}{2r_{coil}^N} \exp\left(-\frac{z}{z_0}\right) (\bar{r})^{N-1} \right] / m_{bit}, \quad (3.16)$$

where v_r is radial velocity and all the gas is assumed to be initially entrained in the current sheet (*i.e.* a “slug” mass distribution). The radial position r is related to the radial velocity by

$$\frac{dr}{dt} = v_r. \quad (3.17)$$

Eq. (3.16) is incomplete, however, as it neglects the radial force of the gas-dynamic pressure that, while initially insignificant when compared to the radial Lorentz force, can eventually equal the pressure of the magnetic field accelerating the current sheet.

3.3.2 An Estimate of the Gas-dynamic Pressure

The radial component of the electromagnetic force on the current sheet is opposed by a gas-dynamic pressure force P_2 that increases as the current sheet moves toward the thruster centerline. This pressure can be estimated assuming the current sheet acts as a normal shock wave:

$$\frac{P_2}{P_1} = 1 + \frac{2\gamma}{\gamma + 1} [\mathcal{M}^2 - 1] \quad (3.18)$$

where P_2 is the pressure of the gas downstream of the shock, P_1 is the pressure upstream of the shock, γ is the ratio of specific heats (taken here to be 5/3), and \mathcal{M} is the local Mach number upstream of the shock:

$$\mathcal{M} = u / \sqrt{\frac{\gamma k T_1}{m_i}} \quad (3.19)$$

where u is the shock velocity (taken to be equal to the current sheet velocity), k is Boltzmann's constant, T_1 is the temperature of the gas upstream of the shock, and m_i is the mass of an ion. While radial current sheet motion could be modeled as an purely isentropic process or as a combination of a shock wave and an isentropic compression, a pure shock wave model is employed here to overestimate the attainable propellant pressure and bound the problem.

The scalar momentum equation for radial motion (Eq. (3.16)) can be modified to include a pressure term:

$$\frac{dv_r}{dt} = \left[P_2 2\pi \bar{r} l_{coil} - \frac{L_C I_1^2 N}{2r_{coil}^N} \exp\left(-\frac{z}{z_0}\right) (\bar{r})^{N-1} \right] / m_{bit}. \quad (3.20)$$

The time-evolution of the pressure P_2 is given by the time-derivative of Eq. (3.18),

$$\frac{dP_2}{dt} = \frac{P_1 2\gamma}{\gamma + 1} \frac{m_i}{\gamma k T_1} 2v_r \frac{dv_r}{dt}, \quad (3.21)$$

bringing the total number of first-order coupled ODEs in the system to nine.

Of the nine equations (Eqs. (3.1), (3.2), (3.3), (3.6), (3.14), (3.15), (3.17), (3.20), and (3.21)), four rely on the semi-empirical relation for coil inductance as a function of current sheet location. It should be noted that no attempt is made here to model energy conversion from radial current sheet motion to axial momentum. The assumption of a slug

mass loading means there was no attempt to model factors such as propellant utilization efficiency that could be a function of coil geometry and would impact the total thruster efficiency.

3.4 Results

Results of the two-dimensional modeling for the four geometries and parameter space studied are shown in Fig. 3.6 along with results from the one-dimensional model where the current sheet does not radially compress. Radial velocities are in the negative r direction, while axial velocities are in the positive z direction.

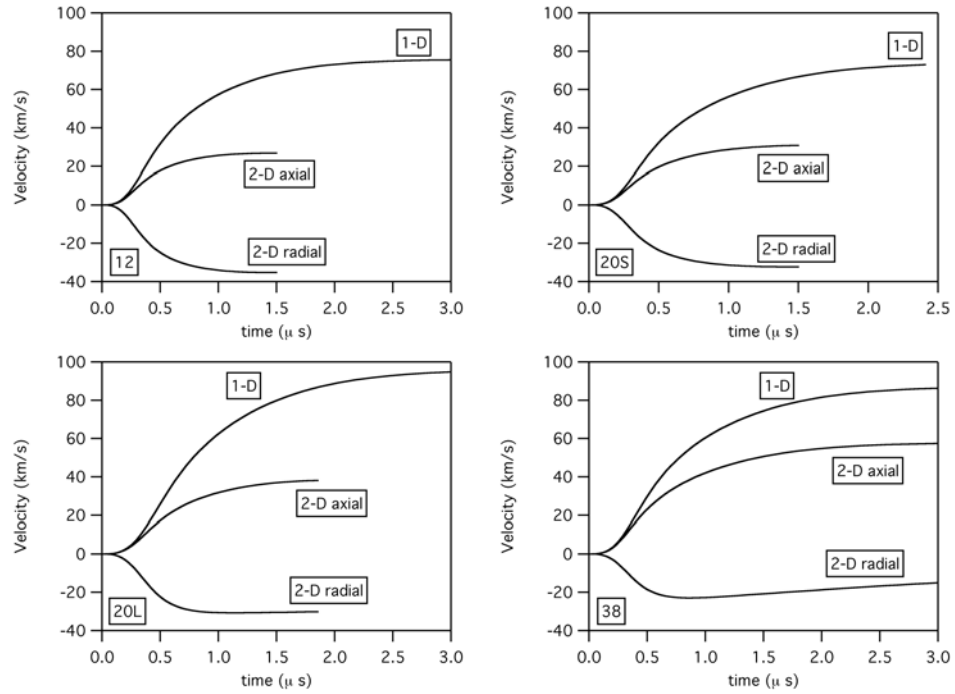


Figure 3.6: Experimental data of simulated compressed current sheets and the corresponding values of $L_{tot}(r, z)$.

The final axial velocity for the case where the current sheet undergoes radial compression is significantly reduced compared to the case where the current sheet does not undergo radial compression. The final exhaust velocities and their percentage decrease as a conse-

Geometry	1-D v_z (km/s)	2-D v_z (km/s)	velocity loss (1-D to 2-D)	KE loss (1-D to 2-D)
12	75	27	64%	87%
20S	73	31	58 %	82%
20L	95	38	60 %	84%
38	86	57	34 %	56%

Table 3.2: Final exhaust velocities for various current sheet geometries.

quence of radial compression is shown in Table 3.2 for the geometries studied.

While there is no mechanism in the present model to convert pressure to axial kinetic energy, it should be noted that the current sheet is continually accelerated axially away from the thruster's upstream surface where a gas-dynamic pressure could potentially act to provide an axial force. Additionally, the operational pressures for a pulsed inductive thruster fall below the range where a physical nozzle could be employed efficiently. To provide an upper bound on recoverable energy, we proceed with a calculation of the energy that, due to propellant compression, might be available for conversion to axial kinetic energy (irrespective of the conversion mechanism).

The energy E in the compressed propellant is calculated as the gas-dynamic pressure P_2 times the volume $\mathbb{V} = \pi \bar{r}^2 l_{coil}$ contained by the current sheet, compressed to the average radius \bar{r} to achieve this pressure :

$$E = P_2 \pi \bar{r}^2 l_{coil} \quad (3.22)$$

The maximum calculated amount of recoverable energy E in the compressed propellant available for conversion to axial kinetic energy is shown in Table 3.3. Also shown in Table 3.3 are re-calculated values of the loss in axial kinetic energy from Table 3.2 to include a recovery of all the gas-dynamic energy in the compressed propellant. These calculated data suggest strongly that the axial directed kinetic energy losses in a conical inductive plasma thruster owing to two-dimensional plasma motion can be detrimental to overall performance.

Geometry	$P_{max}(Pa)$	$\mathbb{V}(m^3)$	$E_{max}(J)$	net E lost (J)	% KE loss
12	8.7e3	2.0e-4	1.7	22.3	80%
20S	1.5e4	3.3e-5	0.44	21.6	80%
20L	1.3e4	3.8e-4	5.1	32.9	73%
38	7.5e3	1.4e-3	2.5	18.5	50%

Table 3.3: Minimum loss of kinetic energy due to radial current sheet compression.

Chapter 4

Model Analysis

THE two-dimensional model developed in Chapter 3 is nondimensionalized and the relevant scaling parameters are identified. The model is solved, followed by a discussion of how the nondimensional scaling parameters affect solution trends.

4.1 Nondimensional Solution Approach

The following substitutions can be made to nondimensionalize the equation set from Chapter 3 following Refs. [14] and [12]:

$$\begin{aligned} I_1^* &= \frac{1}{V_0} \sqrt{\frac{L_C}{C}} I_1 & I_2^* &= \frac{1}{V_0} \sqrt{\frac{L_C}{C}} I_2 \\ V^* &= \frac{V}{V_0} & M^* &= \frac{M}{L_C} \\ v_z^* &= \frac{\sqrt{L_0 C}}{z_0} v_z & z^* &= \frac{z}{z_0} \\ v_r^* &= \frac{\sqrt{L_0 C}}{r_{coil_0}} v_r & r^* &= \frac{r}{r_{coil_0}} \\ t^* &= \frac{t}{\sqrt{L_0 C}} & P^* &= \frac{P}{P_1} \end{aligned} \tag{4.1}$$

Applying these substitutions to Eqns. (3.1), (3.2), (3.3), (3.14), (3.15), (3.20), (3.6),

(3.17), and (3.21) yields the following nondimensional equation set:

$$\begin{aligned}
\frac{dI_1^*}{dt^*} &= \left[L^* V^* + (M^* I_1^* + I_2^*) \frac{dM^*}{dt^*} - \psi_2 L^* I_2^* M^* - \psi_1 L^* I_1^* \right] / (L^* + 1 - M^{*2}) \\
\frac{dI_2^*}{dt^*} &= M^* \frac{dI_1^*}{dt^*} + I_1^* \frac{dM^*}{dt^*} - I_2^* L^* \psi_2 \\
\frac{dV^*}{dt^*} &= -I_1^* \\
\frac{dM^*}{dt^*} &= \frac{N}{2} r^{*\frac{N}{2}-1} v_r^* \exp(-\frac{z^*}{2}) - \frac{1}{2} r^{*\frac{N}{2}} v_z^* \exp(-\frac{z^*}{2}) \\
\frac{dv_r^*}{dt^*} &= \lambda P^* r^* - \phi I_1^{*2} r^{*N-1} \exp(-z^*) \\
\frac{dr^*}{dt^*} &= v_r^* \\
\frac{dv_z^*}{dt^*} &= \alpha I_1^{*2} r^{*N} \exp(-z^*) \\
\frac{dz^*}{dt^*} &= v_z^* \\
\frac{dP^*}{dt^*} &= \Xi v_r^* \frac{dv_r^*}{dt^*}
\end{aligned}$$

(4.2)

4.2 Nondimensional Scaling Parameters

The terms α , ψ_1 , ψ_2 , ϕ , λ , and Ξ appear as the relevant nondimensional scaling parameters of the system in Eqns. (4.2), and are defined as:

$$\begin{aligned}
\alpha &= \frac{V_0^2 C^2 L_C}{2m_{bit} z_0^2} & \psi_1 &= R_e \sqrt{\frac{C}{L_0}} \\
\psi_2 &= R_p \sqrt{\frac{C}{L_0}} & \phi &= \frac{V_0^2 C^2 L_C}{2m_{bit} \bar{r}_{coil_0}^2} \\
\lambda &= \frac{L_0 C P_1 2\pi l_{coil}}{2m_{bit}} & \Xi &= \frac{4\gamma}{\gamma + 1} \frac{m_i}{\gamma k T_1} \frac{1}{\bar{r}_{coil_0}^2 L_0 C} \\
L^* &= \frac{L_0}{L_C}
\end{aligned} \tag{4.3}$$

The parameters ψ_1 and ψ_2 are critical resistance ratios, affecting the damping of the current in the electrical circuit, and L^* is a ratio of the initial (or stray/inaccessible) inductance to the accessible inductance (or inductance change as the distance between the coil and plasma grows). This ratio represents a measure of the fraction of initial stored energy that can be electromagnetically transferred into directed kinetic energy of the plasma. The physical interpretations of these three parameters remains unchanged from those of previous studies of pulsed inductive plasma thrusters with flat inductive coil geometries, and more information on their meanings and implications can be found in Refs. [14] and [12].

Appearing as a new parameter in this model is λ , a measure of the gas-dynamic force opposing radially-inward current sheet motion. Another new parameter arising from two-dimensional motion in the model is Ξ . This parameter provides a relative measure of the growth rate of the gas-dynamic pressure as the current sheet shock front undergoes radial acceleration. For the calculations in the following section, $\psi_1 = 0.05$, $\psi_2 = 0.01$, $L^* = 0.18$, $\lambda = 7.0 \cdot 10^{-7}$, and $\Xi = 2.3 \cdot 10^4$.

The parameter α is referred to in the literature as the dynamic impedance matching parameter, and can be expanded into a product of physically meaningful ratios [14]:

$$\alpha = \frac{C^2 V_0^2 L_C}{2m_{bit} z_0^2} = \frac{1}{8\pi^2} \frac{C V_0^2 / 2}{m_{bit} v_z^2 / 2} L^* \left(\frac{2\pi \sqrt{L_0 C}}{L_0 / \dot{L}_z} \right)^2 \tag{4.4}$$

where $\dot{L}_z = v_z L'_z$ is an average time rate of change in circuit inductance due to current sheet motion and $L'_z = L_C / z_0$ is an average inductance per unit length. The second ratio

on the right hand side of Eq. (4.4) represents the inverse of thrust efficiency and the third term is the inverse of the Lovberg criterion [21]. The numerator of the fourth ratio is the characteristic ringing time of the unloaded ($L_C = 0$) driving circuit while the denominator is the characteristic time that the current sheet remains electromagnetically coupled to the driving circuit. Using this ratio of timescales, the parameter α is understood to be a measure of the dynamic impedance match between the ability of the driving circuit to impart energy to the plasma and the capacity of the axially-moving current sheet to accept that energy in the form of increased acceleration. It has been shown that η_t is maximized in thrusters with $1 < \alpha < 3$, corresponding to driving circuit timescales that are close to the current sheet residence time [18]. This condition allows time for the main current pulse to ionize, drive current in and accelerate the propellant before the time rate of change of the induced magnetic field reverses and energy begins to be removed from the propellant.

The parameter ϕ can be similarly expanded:

$$\phi = \frac{C^2 V_0^2 L_C}{2 m_{bit} \bar{r}_{coil_0}^2} = \frac{1}{8\pi^2} \frac{C V_0^2 / 2}{m_{bit} v_r^2 / 2} L^* \left(\frac{2\pi \sqrt{L_0 C}}{L_0 / \dot{L}_r} \right)^2$$

where $\dot{L}_r = v_r L'_r$ and $L'_r = L_C / \bar{r}_{coil_0}$ have meanings similar to the definitions for α . The second term does not represent thrust efficiency, as in the expansion for α , but rather the inverse of the fraction of total energy that is converted into radial kinetic energy. The fourth term represents a balance between the characteristic circuit time and the characteristic time over which radial (not axial) current sheet motion causes electromagnetic decoupling from the driving circuit.

4.3 Effect of Radial Motion on Thrust Efficiency

Thrust efficiency can be related to α by the following relation:

$$\eta_t = \frac{v_z^{*2}}{2L^*\alpha}.$$

For systems constrained to axial motion (zero radial motion) the optimum value of α for maximum η_t is between one and three [22]. When the current sheet is axially accelerated at a fixed radial position that is less than $\overline{r_{coil_0}}$ (i.e. $v_r^* = 0$ and $r^* = A \forall t^*$ where $0 < A \leq 1$), the absolute value of η_t decreases and the maximum η_t occurs at a higher value of α , as shown in Fig. 4.1. As shown in the figure, the maximum achievable η_t is lower as the sheet is displaced closer to the centerline.

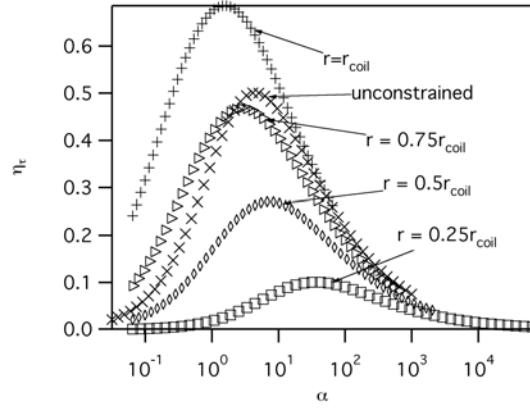


Figure 4.1: Calculated thrust efficiency as a function of α for different radial current sheet displacements.

A possible explanation for the shift in optimum values of α is that as the current sheet displaces radially, it slows the axial acceleration of the current sheet. This causes a longer current sheet residence time in practice, but that information is not contained in α . Consequently, a longer characteristic circuit time, which will increase the value of α , represents a better dynamic impedance match.

Current sheet motion in either the axial or radial direction causes the current sheet to decouple from the inductive coil. If the timescale of radial current sheet decoupling were small compared to the timescale of the driving circuit, radial current sheet displacement

would prevent significant energy transfer into axial current sheet motion. While an efficient coupling of energy into the axial direction is beneficial to thrust efficiency, efficient coupling of energy into the radial direction has a generally detrimental effect on thrust efficiency. This result is not unexpected in light of the assumptions of the model where no means exist to convert the radial motion to axial thrust. Efforts to model such mechanisms are ongoing [23] and outside the scope of the present work. The work presented here models the axial kinetic energy that would be lost due to radial motion to estimate the energy that must be recovered from propellant that is compressed by radial current sheet velocity to maintain the same thrust efficiency as the case of pure axial current sheet acceleration. Therefore, thrust efficiency should be optimized for a condition where the current sheet radially decouples slowly from the inductive coil compared to the timescale of the driving circuit, allowing energy transfer in the axial direction such that axial current sheet displacement causes decoupling from the coil. This implies an increase in η_t for decreasing values of ϕ , a trend that can be generally seen in the plot of η_t versus ϕ for $\alpha = 0.6$, shown in Fig. 4.2.

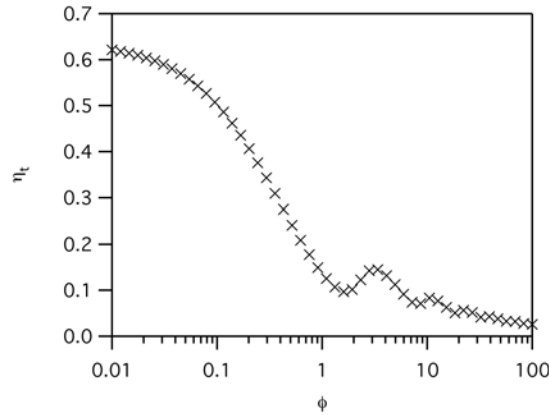


Figure 4.2: Model results of thrust efficiency as a function of ϕ for the unconstrained case with $\alpha = 0.6$.

A contour plot of the combined effects of the two dynamic impedance parameters is shown in Fig. 4.3. As ϕ increases, the thrust efficiency decreases for all values of α due to faster current sheet decoupling from the driving circuit, resulting in lower achievable axial

propellant velocity. The efficiency is optimized at higher values of α as ϕ is increased, in agreement with Fig. 4.1.

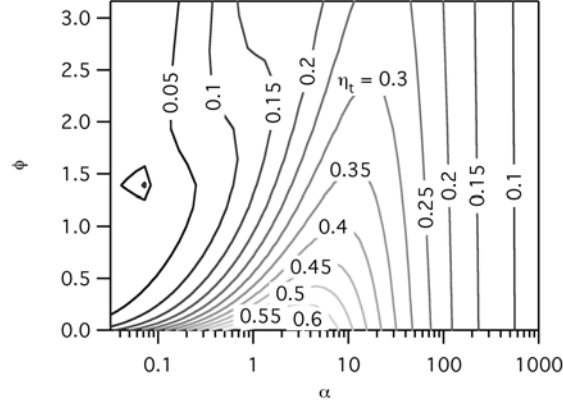


Figure 4.3: Contour plot of thrust efficiency as a function of α and ϕ .

4.4 Summary of Results

Two-dimensional modeling of pulsed inductive current sheet acceleration was presented, and the effect of radial motion on thrust efficiency was discussed. A new scaling parameter ϕ emerged from nondimensionalization of the model that can be interpreted as a radial dynamic impedance parameter. The physical interpretation of this parameter is similar to that of the axial dynamic impedance parameter α from previous studies [14, 18] in that ϕ can be understood as a ratio of the circuit timescale to the timescale of radial decoupling. Results from the model show that:

1. Current sheet displacement in either the radial or axial direction reduces electromagnetic coupling with the coil, causing a decrease in the energy transferrable to both directions of motion.
2. The thrust efficiency for the case of a current sheet that undergoes purely axial translation decreases and the optimum value of α increases as the initial radial position of the sheet is reduced.

3. Further initial radial current sheet displacement (for the case of purely-axial current sheet motion) exacerbates this effect, possibly because radial displacement exacerbates this effect, because the axial decoupling timescale is effectively increased for a radially-displaced plasma.
4. Radial motion also causes an increase in the value of α corresponding to maximum attainable η_t .
5. Radial motion causes a general decrease in thrust efficiency (under the assumptions of the model), with faster radial motion causing a greater decrease.

These results offer insight into the general scaling of inductive plasma thrusters where the current sheet undergoes two-dimensional acceleration. The results are limited by the set of assumptions that guided derivation of the model. Further work beyond the scope of this dissertation could include expansion of the model to include the effects of imperfect current sheet formation, uneven propellant distribution, and plasma dynamics (to name a few).

Chapter 5

Experiment for Measuring Thruster Operating Characteristics

IN this chapter, details about the facility, test hardware, and thruster systems used to gather data on the operating characteristics of a conical theta-pinch pulsed inductive thruster are presented.

5.1 Vacuum Facility

The vacuum facility used in these experiments is a 7.6-m (25-ft.) long stainless steel cylindrical vacuum chamber with a 2.7-m (9-ft.) diameter. A base pressure of 7.6×10^{-5} Pa (5.7×10^{-7} Torr) is maintained by two 2400 l/s turbopumps and two 9500 l/s GHe cryopumps.

5.2 Thrust Stand

The hanging pendulum-type Variable Amplitude Hanging Pendulum with Extended Range (VAHPER) thrust stand [4] directly measures thrust by monitoring the displacement of a thruster from an equilibrium point as a function of time. The stand, capable of supporting

thrusters with masses up to 125 kg and producing between $100\ \mu\text{N}$ and 1 N of steady-state thrust, was recently modified through the addition of a pulsed calibration mechanism to accommodate pulsed thrusters. More information about the thrust stand in its steady-state configuration can be found in Ref. [4].

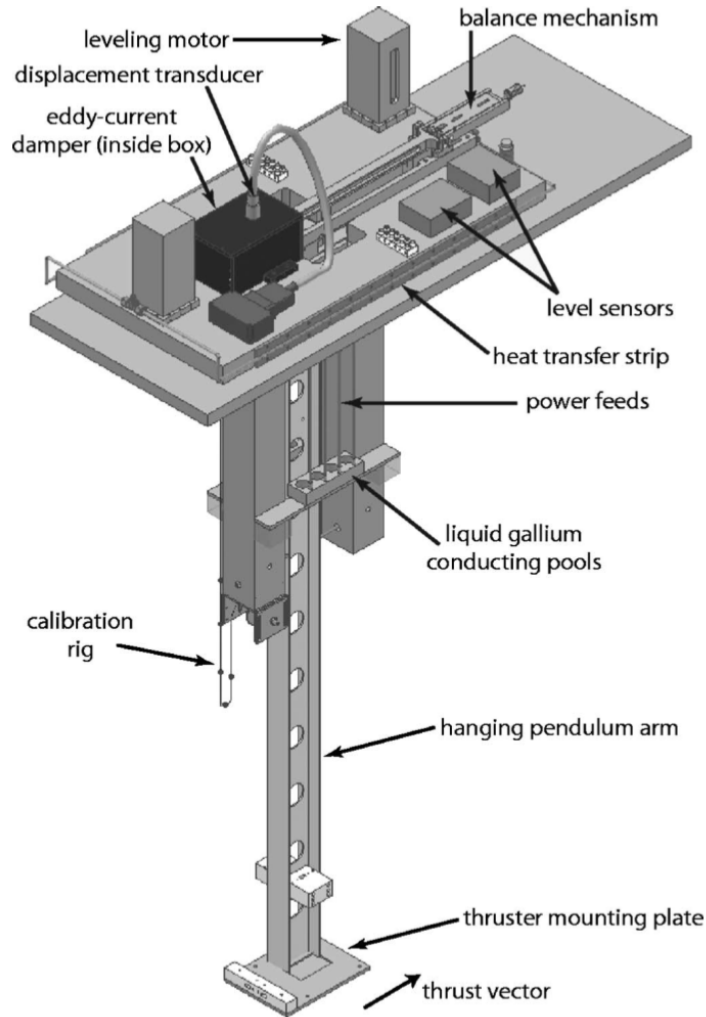


Figure 5.1: VAHPER thrust stand, image from Ref. [4].

Displacement of the thrust stand arm is measured with the use of a linear gap displacement transducer (LGDT). The thrust stand was calibrated for pulsed thrusters by sending a pulse of current through a solenoid mounted to a fixed point not on the thrust stand arm. The electromagnetic field from the solenoid acts against a permanent rare-earth magnet on

the thrust stand arm, repelling it. This force is transmitted to the arm through a piezoelectric force transducer, providing a direct measurement of the pulsed calibration force history. The calibration is achieved by knowing the displacement measured with the LGDT and the force, which can be integrated to yield the impulse bit I_{bit} (impulse per pulse). More information on this setup, shown in Fig. 5.2, and the calibration can be found in Ref. [5].

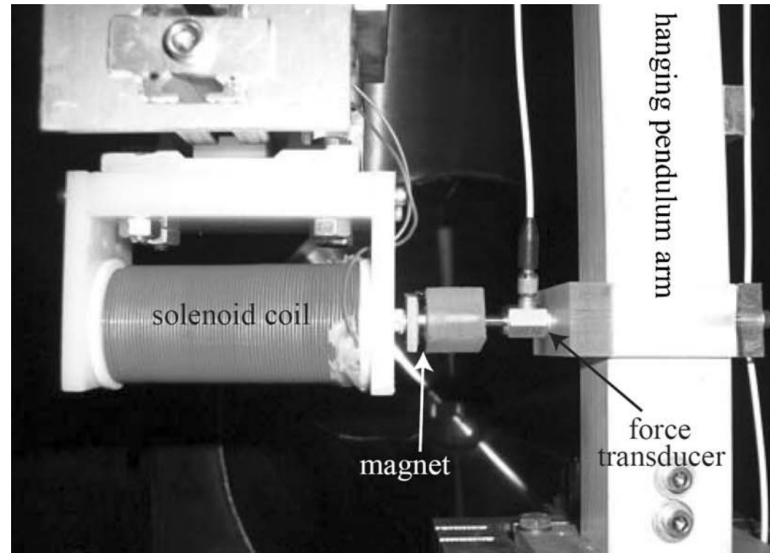


Figure 5.2: Photograph of the thrust stand calibration setup[5].

5.3 The Thruster

5.3.1 Inductive Coil

Two inductive coils were constructed for performance testing with $l_{coil} = 10$ cm (4 in) and $r_{coil} = 4$ cm (1.6 in), one with $\theta = 20^\circ$, the other with $\theta = 38^\circ$. The inductance of both coils is 240 ± 20 nH as measured at the coil leads using an Agilent 4285A precision LCR meter. The coil with $\theta = 38^\circ$ is shown in Fig. 5.3 prior to being encased in RTV to insulate the coil surface from the ionized propellant. This insulating layer was covered with aerosol boron nitride to prevent ablation of the coil surface.

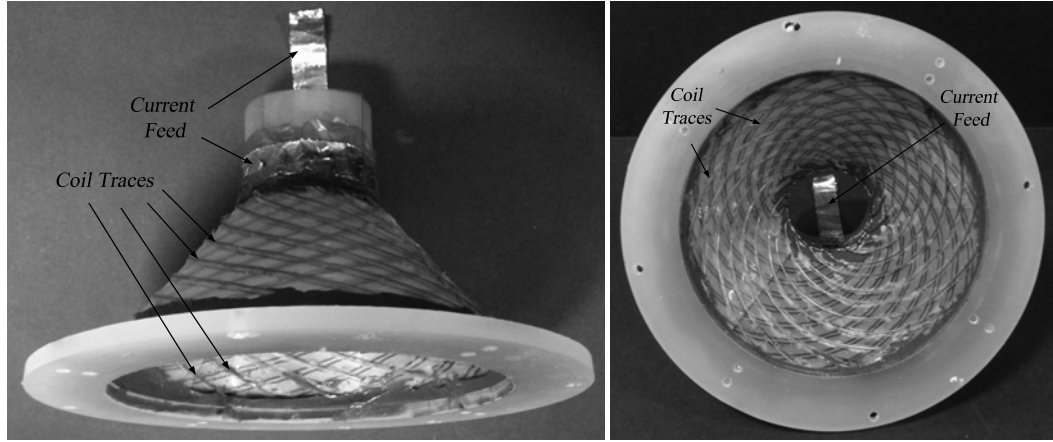


Figure 5.3: Photographs of the inductive coil taken *Left*: from the top and *right*: along the thrust axis.

The coils were designed to be like the PIT, possessing conducting paths in two layers that, when superimposed, create a purely azimuthal current at the coil face. Kapton-insulated 22 gauge wire carries the current, with sixteen single-turn (half-turn per layer) windings comprising the coil and connected in parallel to a common, circular current feed of one-inch wide, twelve gauge flat copper speaker wire. The circular current feed has an axial cut at one azimuthal location to interrupt any induced azimuthal eddy currents in the feed. The two conducting layers are separated by two layers of 0.25 mm (0.01 in) thick mylar.

5.3.2 Preionization and Propellant Injection

The capacitors in some inductive accelerators, like the PIT [1, 2, 3], must be charged to high voltages so that the discharge current through the inductive coil can first ionize the propellant. One way to alleviate this high voltage requirement is to partially ionize the propellant in front of the inductive coil to permit inductive interaction and energy transfer to the propellant [18], allowing for a lower initial voltage level on the energy storage system.

The use of preionization in pulsed inductive devices is ubiquitous throughout the literature with a wide range of applications including plasma fusion and spacecraft propulsion.

For example, preionization has been successfully employed by striking a glow discharge between two electrodes [9, 24, 25], sending a separate lower-energy pulse through an inductive coil [10, 11, 26], and creating a radio frequency plasma [1, 27].

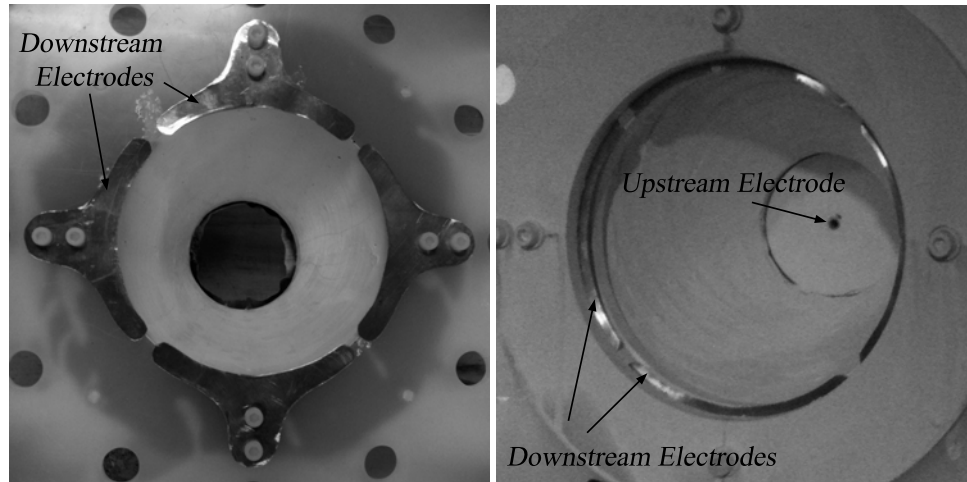


Figure 5.4: Photographs of *Left*: the downstream electrodes with a cover removed and *Right*: both electrodes with the cover attached.

Preionization was employed in the thrusters studied here to lower the voltage requirements of the driving circuit, simplifying construction of the experimental setup with respect to capacitor and switch voltage requirements and the voltage level the electrical insulation needed to withstand. The driving circuit for the preionizer consisted of a low-current AC power supply powered by a 12 V battery. The output of the AC supply was fed through a rectifier to apply a DC voltage to the electrodes. The resulting voltage after breakdown was 300 V. An unfiltered 16 second exposure of the preionizer operating on 150 mg/s of argon is shown in Fig. 5.5.

A glow discharge was initiated prior to the main current pulse through the inductive coil between electrodes located at the upstream and downstream ends of the coil as shown in Fig. 5.4. The downstream electrodes are composed of copper and were segmented so as to avoid presenting a continuous azimuthal conductive path that could support eddy currents, drawing energy from the discharge. The upstream electrode was a six inch long section of 0.635 mm (0.25 inch) stainless steel tubing through which propellant was injected.

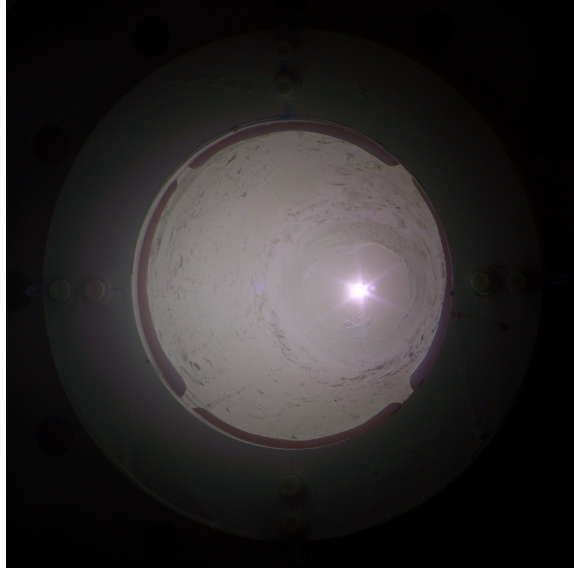


Figure 5.5: Unfiltered 16 second exposure of the preionized propellant at $\dot{m} = 150$ mg/s.

Propellant flowed to the upstream electrode through a polyethylene tube that breaks the electrical connection of the electrode to ground. Mass flow rate was measured with an MKS metal-sealed type 1479A flow controller with maximum flow rate of 10,000 sccm. Argon propellant was used for all data presented here.

5.3.3 High Power Switch and Capacitor Bank

A simple mechanical switch, shown in Fig. 5.6 discharged the capacitor bank, also shown in Fig. 5.6. The switch was designed to minimize inductance, adding less than 50 nH to the driving circuit. The switch was located external to the vacuum vessel and was activated manually. Measurement of the fast-rising current pulse that resulted from closing the switch was used as a trigger for all data acquisition.

The capacitor bank consisted of four 10 μ F capacitors rated to 7.5 kV. The capacitors were connected in parallel, decreasing the inductance they presented to the driving circuit and increasing the total capacitance to 40 μ F. Stripline constructed from 1 inch wide 12 gauge flat speaker wire was used to connect the capacitor to the switch and thruster.

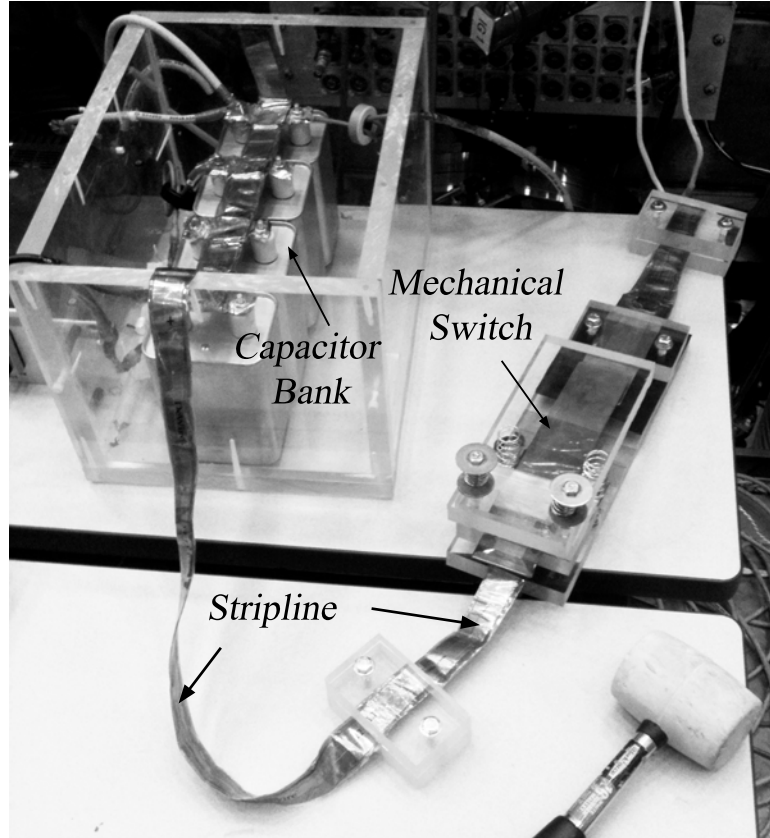


Figure 5.6: Photograph of the capacitor bank and mechanical switch.

5.4 Experimental Setup

The thruster was mounted onto the thrust stand as shown in Fig. 5.7. The capacitor bank and switch were located outside of the chamber to reduce the challenge of holding-off high voltage and allow access to the mechanical switch. Parasitic inductance was minimized where possible with the use of stripline to connect all components of the system. Differential voltage measurements at the thruster leads indicate that a little over three tenths of the capacitor bank charging voltage is applied across the thruster. This indicates that due to the parasitic inductance the efficiency can be no greater than $\sim 31\%$ with this particular thruster and power feeding configuration [3]. Results from performance testing using this un-optimized setup appear in the next chapter.

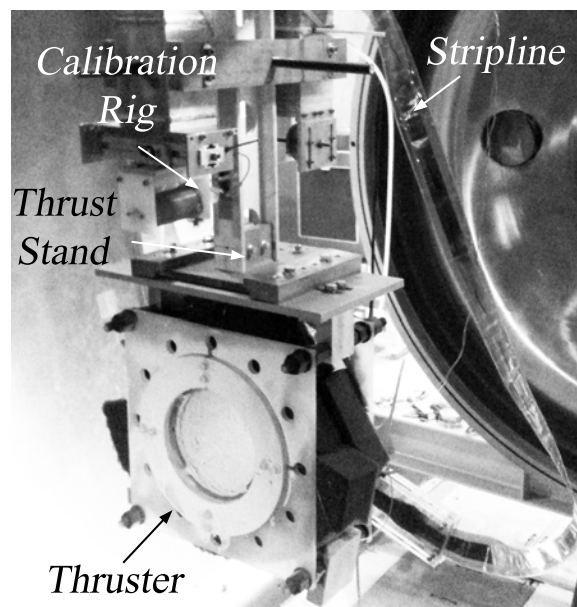


Figure 5.7: Thruster mounted on the thrust stand.

Chapter 6

Measurements and Analysis of Thruster Operating Characteristics

RESULTS of the experiment described in Chapter 5 are presented and discussed, beginning with measurements of the capacitor bank voltage and current as a function of time, followed by thrust measurements and time-integrated photographs of the discharge.

6.1 Capacitor Bank Voltage and Driving Current

Typical capacitor bank voltage V_0 and circuit current measured during a typical discharge event appear in Fig. 6.1 as a function of time.

The voltage at the thruster terminals during a pulse was measured using a differential voltage probe at capacitor bank voltages of 100, 200, and 300 V and is shown in Fig. 6.2. The peak-to-peak voltage limits on the differential probe limited the voltage range over which this test could be performed. The fraction of bank voltage that appeared across the thruster terminals during the discharge was $\sim 31\%$ in all three cases. If this linearity is assumed to extend up to 5 kV, then the maximum voltage that could appear during a pulse across the thruster in the present configuration is 1.55 kV.

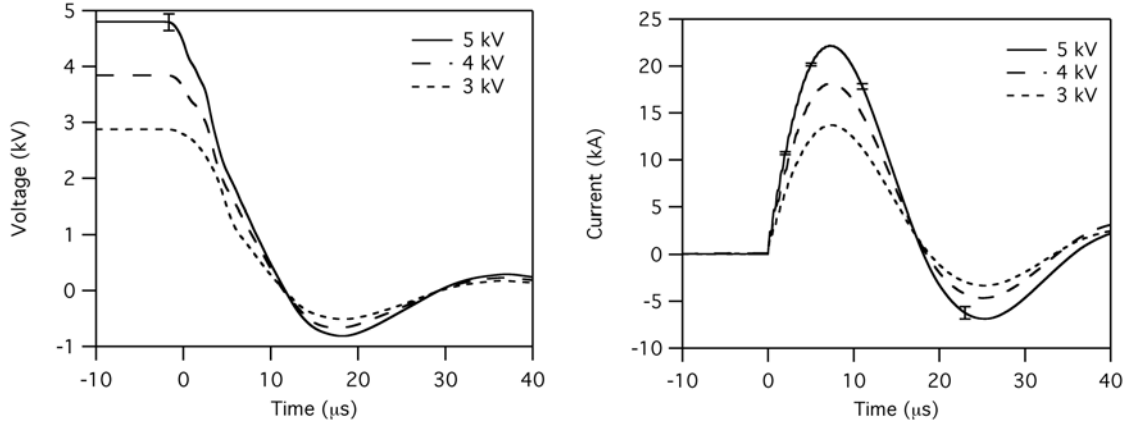


Figure 6.1: Typical capacitor bank discharge voltage and circuit current as a function of time with representative error bars shown.

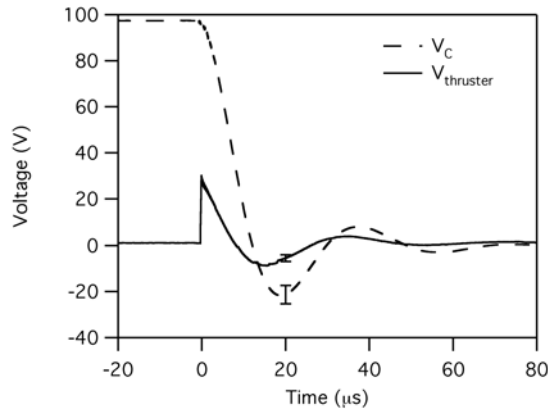


Figure 6.2: Voltage measurements at the capacitor bank and at the thruster terminals during discharge for $V_0 = 100V$ with representative error bars shown.

6.2 Impulse Calculations

The displacement of the thrust arm produced by two thrusters, one with a 20° half cone angle (designated as thruster 20L) and the other with a half cone angle of 38° (designated thruster 38) was measured for various values of V_0 and mass flow rates \dot{m} as a function of time. The total change in thrust arm velocity was calculated by fitting an analytical function to the displacement measurements and evaluating the derivative at the time of thruster operation, which was assumed to be impulsive on the timescale of thrust arm movement. The total impulse was calculated from measurements of thrust stand arm displacement using

an independent calibration factor determined by applying known impulse bits to the thrust stand.

6.2.1 Effective Mass Calculation: Thrust Stand Calibration

Deflection of the thrust stand arm is measured with an LGDT as mentioned in Chapter 5 Section 5.2. An impulse is imparted to the thrust stand arm by a current pulse through solenoid coil mounted to a static portion of the thrust stand. The electromagnetic field from the solenoid acts against a permanent magnet mounted to a force transducer. This force transducer is attached directly to the movable thrust stand arm and permits measurement of the force applied during a calibration pulse. The force is recorded and integrated to calculate the total I_{bit} imparted to the thrust stand arm. A representative force transducer measurement and the commensurate impulse appear in Fig. 6.3.

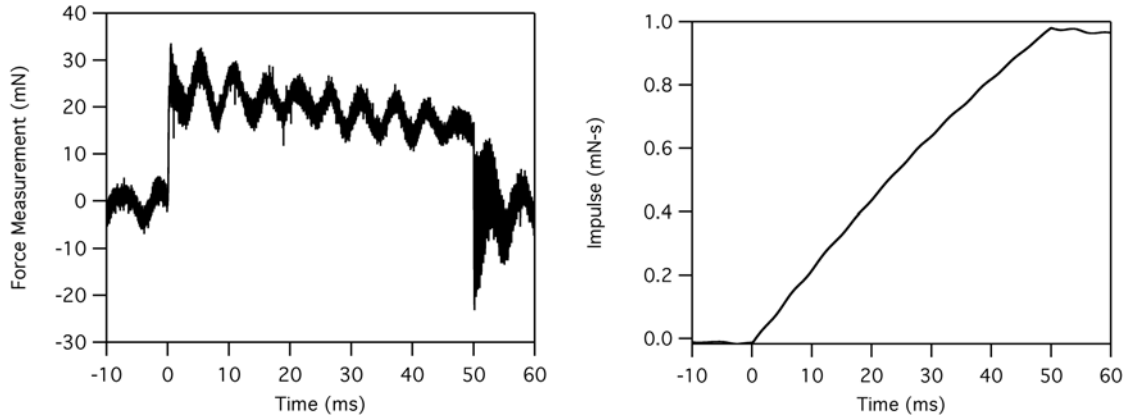


Figure 6.3: Signal from the force transducer and its time integral.

The displacement of the thrust stand arm before and after the time of impact is fitted using an exponentially-decaying sinusoidal function, yielding analytical expressions that can be differentiated to obtain the velocity of the arm. The discontinuous impulsive change in the velocity produced by the pulse can be found by evaluating the difference in the position derivatives at $t = 0^-$ and $t = 0^+$. By assuming the stand acts as an ideal spring-mass-damper system, and that the force is impulsive (duration of force \ll thrust stand

arm period), it follows that the impulse and change in thrust stand arm velocity (and also momentum) are linearly related [28]. The LGDT signal and the curve fit of the motion for $t > 0$ is shown in Fig. 6.4.

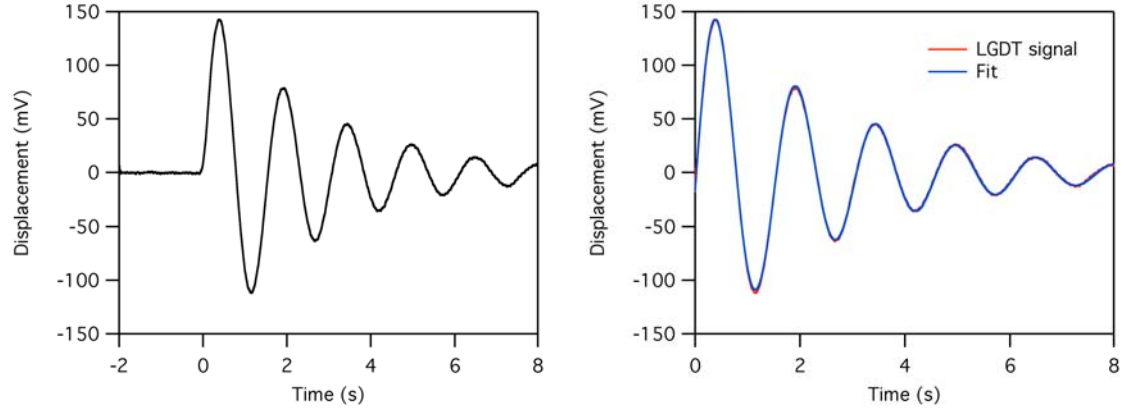


Figure 6.4: *left*: An LGDT signal resulting from an applied impulse and *Right*: a comparison of the signal to a fitted damped sinusoidal waveform for $t > 0$.

The change in velocity is calculated for various values of I_{bit} and the constant of proportionality is taken to be the effective mass of the thrust stand arm. A correction is made to the effective mass calculation to account for the difference in the distance from the force transducer and the centerline of the thruster to the pivot point of the thrust stand arm. The pivot point is 66 cm (26 in) above the force transducer and 97.5 cm (38.4 in) above the centerline of the thruster.

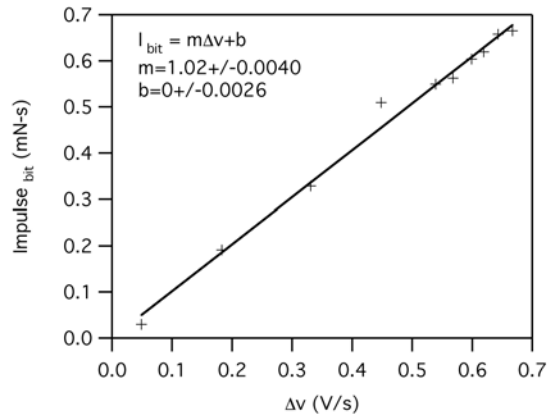


Figure 6.5: A plot of I_{bit} versus momentum imparted to the thrust stand by the solenoid.

6.2.2 Thrust Arm Displacement Measurements

Thrust arm displacement measurements are shown in Fig. 6.6 for thruster 20L and thruster 38 while curve fitting results are shown overlaying these measurements for $t > 0$ in Fig.6.7.

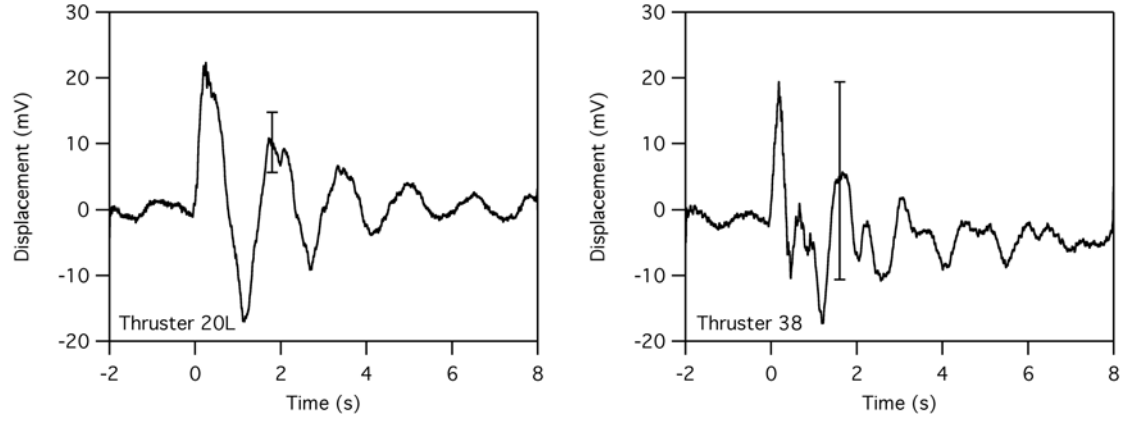


Figure 6.6: Thrust arm displacement measurements for thruster 20L and thruster 38 for V_0 5 kV and $\dot{m} = 120$ mg/s with typical error bars shown.

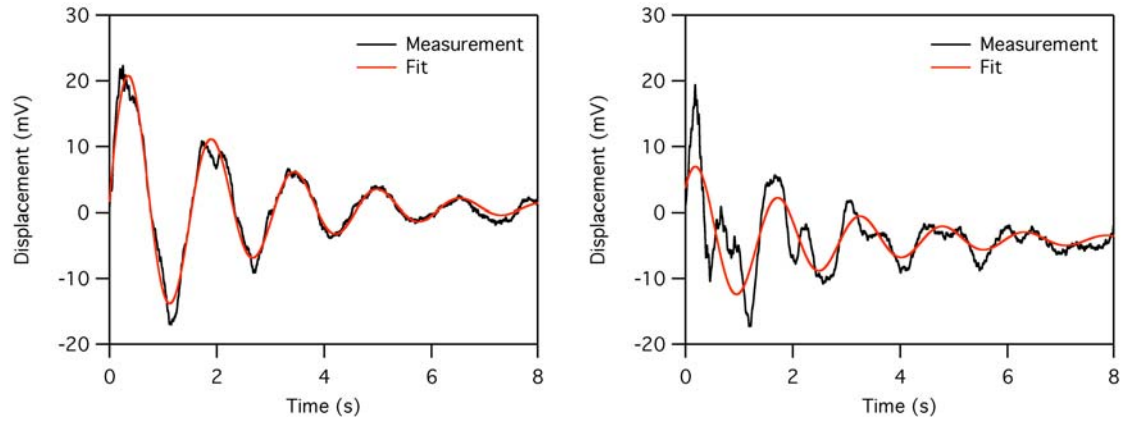


Figure 6.7: Curve fitting results thrust arm displacement measurements for thruster 20L and thruster 38 for for $t > 0$, V_0 5 kV, and $\dot{m} = 120$ mg/s.

While curve fitting results for displacement measurements of thruster 20L represent the data well, displacement measurements for the thruster with a 38° half cone angle (designated as thruster 38) appear to be distorted by signal noise, resulting in a poor curve fit. Both signals are weak, however measurements for thruster 20L can be fitted to a damped sinusoidal function and analyzed to obtain a value of I_{bit} . The displacement data of thruster

38 are too low in amplitude to be reliably analyzed in this way. These measurements reveal that the displacement of the thrust stand due to the impulse imparted by thruster 20L is larger than the displacement from operation of thruster 38.

6.2.3 Impulse Calculation

All data that follow were obtained using argon propellant. Results of calculations for I_{bit} of thruster 20L are shown in Fig. 6.8 for various values of \dot{m} obtained at $V_0 = 5$ kV. The calculated value for the I_{bit} attains a maximum value of 0.097 mN-s for $90 < \dot{m} < 150$ mg/s.

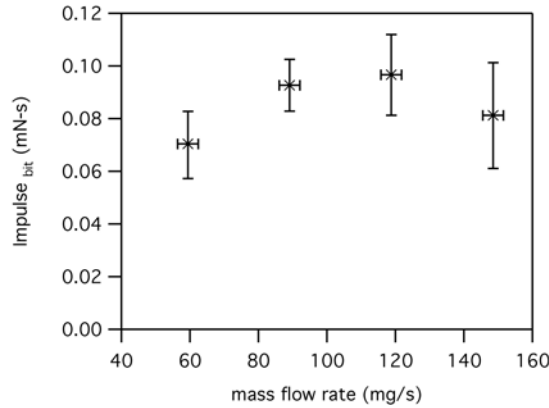


Figure 6.8: I_{bit} for thruster 20L as a function of \dot{m} with $V_0 = 5$ kV.

The base pressure in the vacuum vessel is shown in Fig. 6.9 as a function of \dot{m} . For values of \dot{m} greater than 150 mg/s, the base pressure rose above 1 mTorr, which implies that the back pressure in the tank is great enough to exert a detrimental drag force on an exhausting current sheet. the higher pressure also increases the voltage insulation requirements along the stripline feeding power to the thruster from outside the vessel.

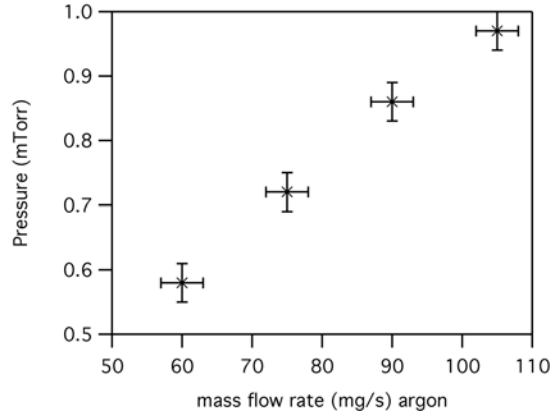


Figure 6.9: Base pressure in the vacuum vessel as a function of \dot{m} .

6.3 Photographic Evidence

All photographs of thruster operation were unfiltered and obtained using a Kodak Z812 IS SLR digital camera with an ISO setting of 64, a focal ratio of 8 and an exposure time of 1 second. All image-altering functions of the camera, including white balance and automatic focusing, were disabled. The camera was pointed at the thruster, offset approximately 10 degrees from the thruster centerline located 6 m (20 ft) downstream from the thruster exit plane.

Images of the preionization were obtained and digitally subtracted from images of the plasma during a main current pulse through the coil to remove any ambiguity regarding the source of the light with respect to these two separate processes. Results from previous studies [29, 30, 31] have shown that light intensity qualitatively agrees well with regions of higher current density. Assuming this to be the case here as well, we draw conclusions about trends in current sheet location based on the brightness of light in photographs. It cannot be overstated that any conclusions reached using these time-integrated, unfiltered photographic data are restricted to qualitative trends only (in recognition of this uncertainty).

Photographs of thruster 20L operating on 120 mg/s are shown in Fig. 6.10 for three different values of V_0 . As V_0 is decreased, the brightness of the discharge also decreases,

suggesting (not surprisingly) that as V_C decreases a smaller current density is driven in the preionized propellant. Also with decreasing V_0 , the location of the brightest light in the photograph moves downstream (towards the exit of the cone).

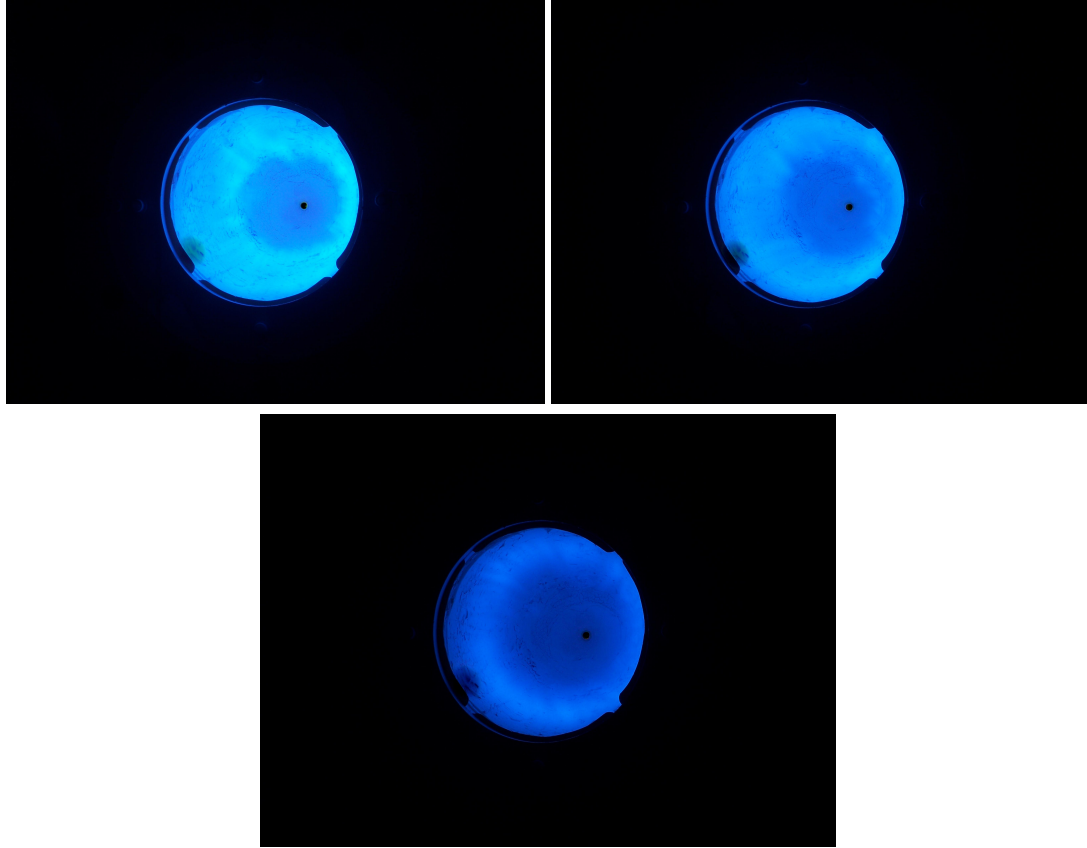


Figure 6.10: Time-integrated photographs of thruster 20L operating on 120 mg/s with *Top Left*: $V_0 = 5$ kV, *Top Right*: $V_0 = 4$ kV, and *Bottom*: $V_0 = 3$ kV.

A previous study [32] showed that the current sheet formation process depends on a ratio of the voltage appearing at the thruster (which is directly proportional to V_0) to the propellant pressure, indicating the existence of a Townsend-like breakdown process. For this type of breakdown, the electrons attain energies well above those necessary for ionization at lower values of \dot{m} (lower values of neutral density), but undergo fewer ionizing collisions with the background neutrals. As the value for \dot{m} is raised, the number of collisions between electrons and neutral particles increases, however the energy gained by the electrons from the electric field (created by the current pulse) between collisions decreases

due to a shortened electron-neutral mean free path. At values of \dot{m} above the optimum, the ionization rate becomes limited by the amount of energy the electrons are able to acquire between collisions as opposed to values below the optimum where the ionization rate is limited by the availability of target neutral particles. These competing effects lead to the existence of an optimum ratio of electric field (proportional to V_0) to pressure (proportional to \dot{m}).

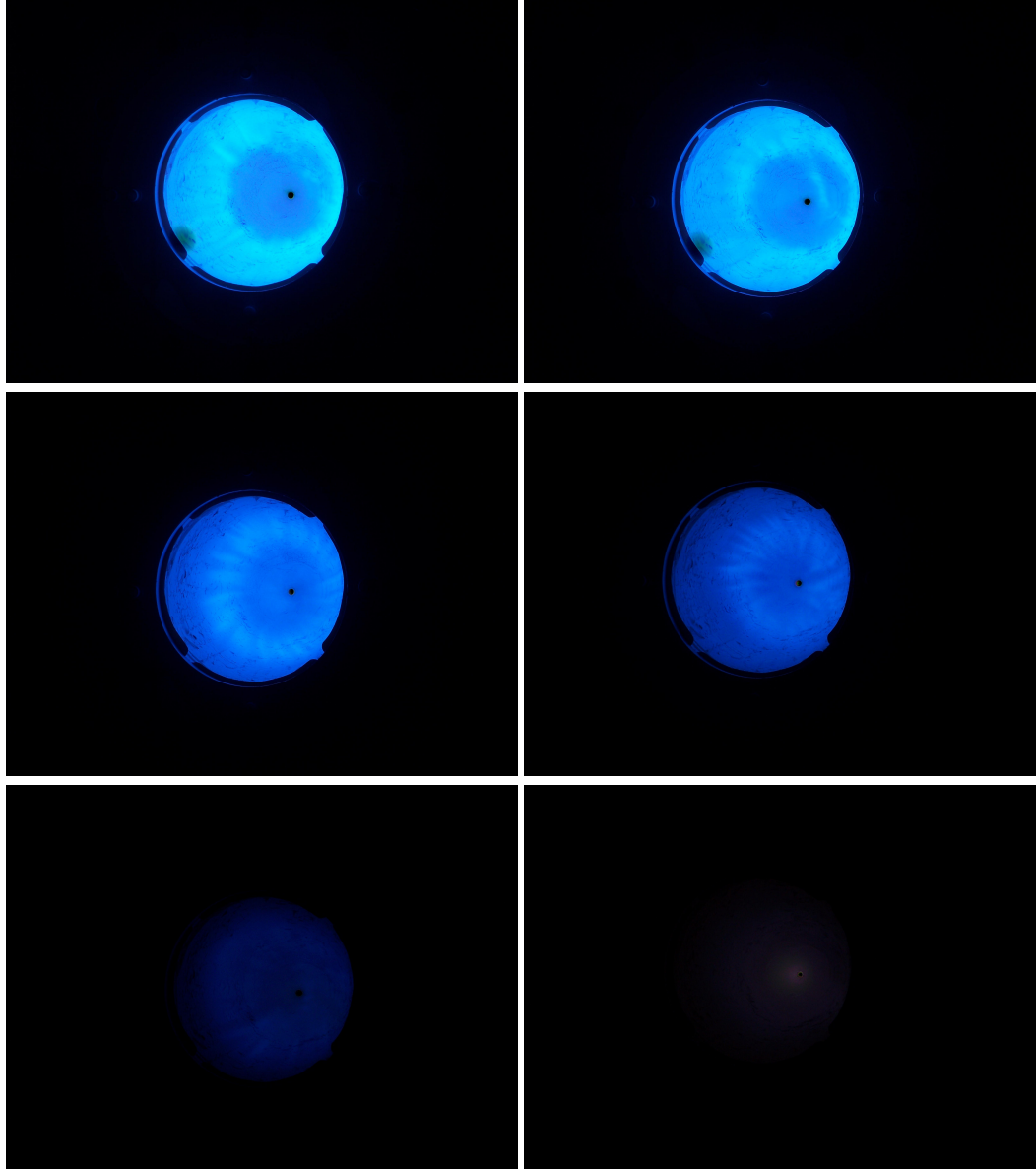


Figure 6.11: Time-integrated photographs of thruster 20L operating on (from left to right, top to bottom) 150, 90, 30, 18, 15, and 12 mg/s with $V_0 = 5$ kV.

Propellant injection occurs at a single point along the centerline of the thruster at the upstream end of the coil and diffuses axially downstream into the vacuum vessel, leading to a lower pressure at the downstream end of the coil as compared to the upstream end. If this trend in light intensity is representative of a similar trend in current density, a possible explanation is that as V_0 is lowered, the optimum pressure for current sheet formation is also lowered, leading current sheet formation to be preferentially shifted towards the downstream end of the coil.

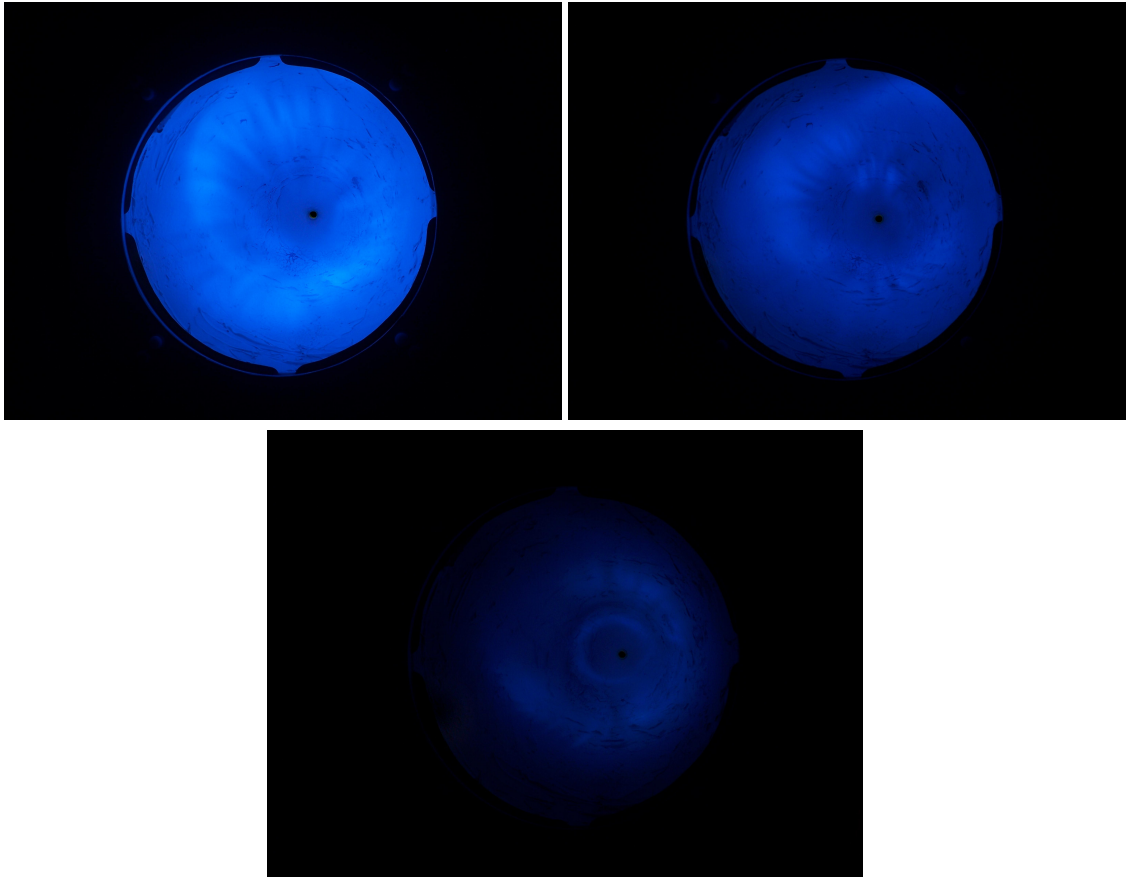


Figure 6.12: Time-integrated photographs of thruster 38 operating on *Top Left*: 120 mg/s, *Top Right*: 90 mg/s, and *Bottom*: 45 mg/s with $V_0 = 5$ kV.

Photographs of thruster 20L operating on argon with decreasing \dot{m} are presented in Fig. 6.11 for $V_0 = 5$ kV. As \dot{m} is decreased, the brightness of the discharge also decreases, suggesting as in the case for decreasing V_0 that a smaller current density is driven in the

preionized propellant. Also as \dot{m} decreases, the location of the brightest light moves either radially inwards or upstream towards the point of propellant injection. If this trend in light intensity is representative of a similar trend in current density, a possible reason for this trend is that as \dot{m} is lowered, the optimum pressure for current sheet formation moves upstream and towards the centerline of the thruster. The decrease in overall light intensity could indicate that a smaller fraction of the total volume of propellant lying within the region of significant electromagnetic interaction with the inductive coil has a pressure close to the optimum value, with a higher fraction of the propellant volume at a pressure significantly lower than the optimum value.

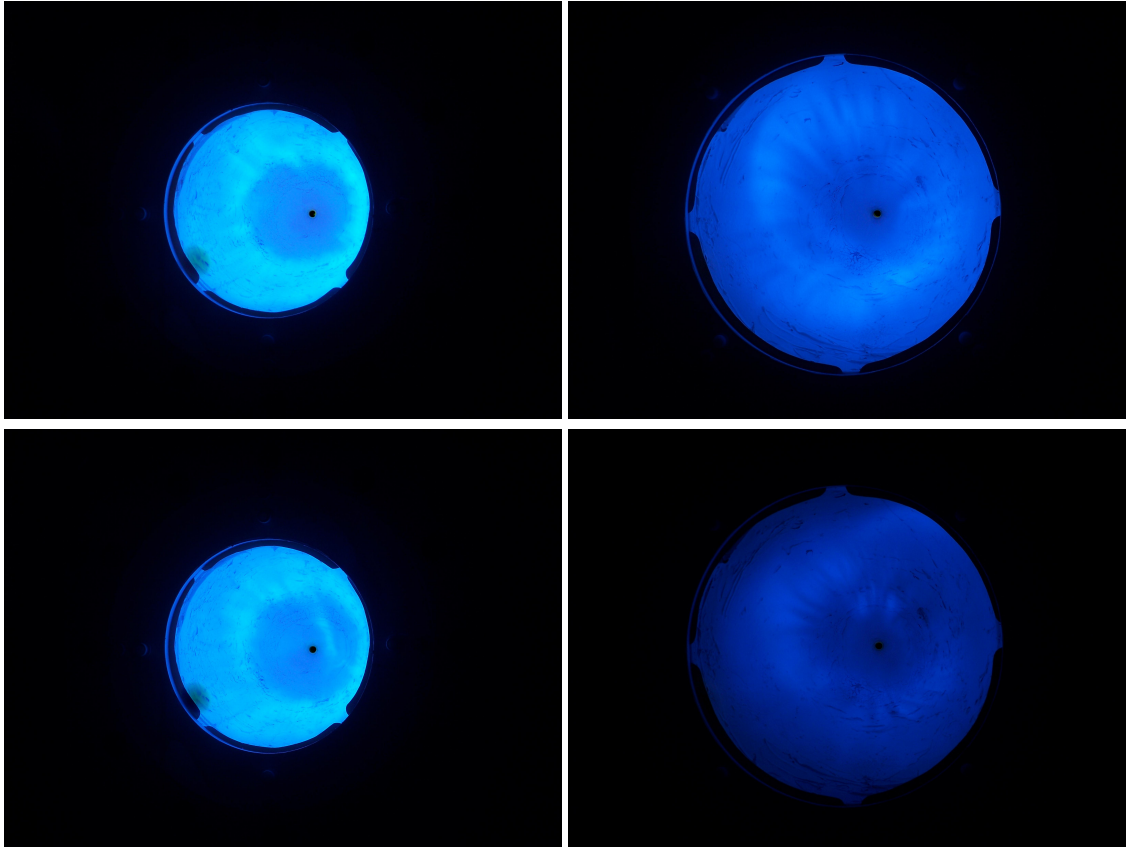


Figure 6.13: Time-integrated photographs of thruster 20L and 38 operating on *Top*: 120 mg/s and *Bottom*: 90 mg/s with $V_0 = 5$ kV. Photographs were obtained at the same zoom level and camera orientation with respect to each thruster.

Photographs of thruster 38 operating with $V_0 = 5$ kV for decreasing values of \dot{m} are

shown in Fig. 6.12. The brightness of the discharge decreases and the brightest sections of the discharge move either towards the centerline of the thruster or the upstream end of the coil with decreasing \dot{m} , just as they did for thruster 20L. A similar conclusion could be drawn (as in the case of thruster 20L) that if light intensity represents current density at that location, current sheet formation is hindered along the coil face due to a paucity of target neutral particles for ionization at that location. The current sheet may be forming either in a restricted volume at the upstream end of the thruster or at a location radially-displaced from the coil. Both of these situations would result in decreased energy coupling from the coil to the propellant.

Two rows of photographs of thruster 20L and 38 operating at the same values of V_0 and \dot{m} for each row are shown in Fig. 6.13. The photographs were obtained at the same zoom level and camera orientation with respect to each thruster. The discrepancy in the apparent size of the bright region is due to the larger major radius of thruster 38, which has the same minor radius and coil length as thruster 20L but a larger cone angle. The discharge in thruster 20L appears brighter than the one in thruster 38 for both values of \dot{m} . The brightness of the discharge in thruster 38 for $V_0 \geq 4kV$ and $\dot{m} = 120$ mg/s appears similar to that of photographs of thruster 20L at $V_0 \leq 3$ kV and $\dot{m} \leq 18$ mg/s.

Chapter 7

Summary and Conclusions

A summary of analytical results from the modeling study is presented first, followed by a summary of experimental results and finally a comparison of the two sets of findings.

7.1 Summary of Analytical Modeling Results

A semi-empirical expression for the dependence of coil inductance on current sheet position in two dimensions was developed, and its utility was demonstrated by using it to expand a one-dimensional circuit-based acceleration model to two dimensions. The two-dimensional function for coil inductance can be readily adapted to any coil geometry by experimentally measuring the inductance profile as a function of current sheet position and curve-fitting for three parameters (L_C , z_0 , and N). While it is possible that there may be a relation encompassing all of these parameters that would obviate the need for experimental determination of the inductance profile, finding that solution is beyond the scope of the present work. The two-dimensional function can be tailored to a coil geometry by using a simulated current sheet to measure the inductance as a function of axial current sheet position at zero radial displacement, and conversely by measuring the inductance as a function

of radial current sheet position at zero axial displacement. Magnetic field modeling can be substituted for experimentally-obtained inductance measurements.

Once incorporated into the circuit model, this two-dimensional relation for inductance allows the calculation of axial and radial Lorentz body forces at an averaged current sheet location. Estimation of how the gas-dynamic pressure of the propellant is affected by current sheet propagation permits the writing of a radial momentum equation that can be solved to obtain the radial acceleration of the current sheet. When this model is applied to the parameter space for low power conical pulsed inductive thrusters, the results indicate that radial displacement acts to rapidly decouple the current sheet from the driving coil, leading to a reduction in axial acceleration and associated axially-directed kinetic energy as compared to the case of pure axial displacement. An estimation of the available potential energy in the compressed propellant shows that even if this energy could be transferred into axial kinetic energy, the losses due to increased entropy are substantial. These results would not be applicable to other types of inductively-created plasmas, such as those with a closed magnetic field profile, which involve significantly increased plasma temperatures over those achieved in a low-power pulsed inductive thruster.

Nondimensionalization of the model resulted in several dimensionless scaling terms, including the axial and radial dynamic impedance parameters. Contour plots of thrust efficiency as a function of these two parameters were presented. Trends in these plots indicate that as the radial dynamic impedance parameter ϕ is increased, thrust efficiency is optimized at greater values of the axial dynamic impedance parameter α . This is explained by a longer axial acceleration timescale due to radial current sheet displacement reducing the axial current sheet acceleration. The longer axial acceleration timescale causes a better dynamic impedance match to occur for a longer characteristic circuit timescale. This change in optimum α should be considered when comparing experimental measurements of the performance of thrusters with different coil geometries where, for the same experimental conditions, a change in thruster performance measurements could be due either to an effect

of changing the coil geometry or changing the impedance matching.

In the present model with no mechanism to convert radial kinetic energy to directed axial thrust, efficiency is maximized for smaller values of the radial dynamic impedance parameter. This indicates that higher axial current sheet velocity is achieved when the current sheet decouples slowly in the radial direction compared to the characteristic pulse timescale of the driving circuit.

The major findings based upon results of the two-dimensional model are:

1. Current sheet displacement in either the radial or axial direction reduces electromagnetic coupling with the coil, causing a decrease in the energy transferrable to either direction of motion.
2. The thrust efficiency for a current sheet that undergoes purely-axial translation decreases monotonically as the initial radial position of the sheet is reduced.
3. Radial motion of the current sheet decreases the amount of initially-stored energy electromagnetically coupled into axially-directed kinetic energy in the current sheet.
4. Calculated values of the gas-dynamic energy contained in propellant compressed by radial current sheet motion are lower than the reduction in current sheet axial kinetic energy resulting from radial motion, implying that entropic energy losses could be significant.
5. Radial current sheet motion has a generally detrimental effect on thrust efficiency
6. Faster radial current sheet decoupling increases the value of α at which maximum thrust efficiency occurs and decreases the value of thrust efficiency.

The range of applicability of these results may extend to all power regimes of this thruster class as the energy conversion process required to recover energy invested in radial current sheet acceleration (from electrical to thermal and subsequently from thermal to

mechanical) is necessarily less efficient than direct axial current sheet acceleration (a direct conversion from electrical to mechanical energy). On the other hand, even if radial compression represents a loss in axial kinetic energy, the extent to which the conical geometry increases the propellant utilization efficiency remains to be quantified.

7.2 Summary of Experimental Results

Experiments were performed to evaluate the operating characteristics of two pulsed inductive conical theta pinch thrusters with inductive coils of two different half cone angles operating with a separate preionization system. One thruster had an inductive coil with a half cone angle of 20° (designated thruster 20L) and the other had an inductive coil with a half cone angle of 38° (designated thruster 38).

Thrust stand displacement measurements were performed for both thrusters. The signal level for both thrusters was small, with the ratio of the displacement measurement to the noise in the data acquisition system only sufficiently large for reliable calculation of the impulse bit produced by thruster 20L. This indicates that thruster 20L produced more axial thrust compared to thruster 38, however the fact that the generated impulse was small may indicate that the difference in thrust levels was due to an inefficient current sheet formation process rather than an inefficient current sheet acceleration. Measurements indicate that thruster 20L produces a maximum impulse bit at a mass flow rate of argon between 90 and 150 mg/s at a capacitor charging voltage of 5 kV, suggesting a dependence of current sheet formation on a Townsend-like breakdown process as described in a previous study [32].

Time-integrated, unfiltered photographs were obtained for both thrusters mounted on the thrust stand during operation. Trends in the brightness of the images were assumed to qualitatively represent the current sheet locations following previous studies where this was shown to be a reasonable assumption [29, 30, 31]. Thruster 20L produced a brighter image than thruster 38 for the same operating conditions. Brightness of the photographs

also increased with increasing mass flow rate for both thrusters and increasing capacitor charging voltage in thruster 20L.

As the mass flow rate was decreased, the location of highest light intensity moved either radially inwards or upstream towards the point of propellant injection for both thrusters. As capacitor charging voltage decreased, the location of highest light intensity moved downstream for thruster 20L. The simple propellant injection scheme employed in the experiment likely led to a gradient in propellant pressure in the volume bounded by the inductive coil. A previous study showed that values of current sheet brightness and current density produced by an inductive coil operating in a backfilled environment achieve a maximum with respect to a ratio of the voltage applied across the inductive coil and the ambient pressure [32]. If light intensity can be assumed to be a good representation of current sheet location, then a possible explanation for the trend in light intensity is that as the mass flow rate is reduced, the location of optimum propellant pressure for current sheet formation (the pressure that corresponds to the brightest and densest current sheet) moves upstream towards areas of higher relative propellant pressure. As the capacitor voltage is decreased, the propellant pressure also decreases to maintain the same optimum ratio of capacitor voltage to pressure for current sheet formation, shifting current sheet formation downstream towards areas of lower propellant pressure. The brightest areas of the brightest images of both thrusters do not appear at the downstream end of the thruster.

The major results based upon experimental findings are:

1. At the same operating conditions, the thruster with an inductive coil possessing a smaller half cone angle demonstrated higher thrust.
2. Calculated values of impulse bit from the thrust stand measurements were only statistically significant in thruster 20L due to a small signal to noise ratio for thruster 38. The impulse bit for thruster 20L reached a maximum measured value of 0.097 mN-s in the flow rate range of $90 < \dot{m} < 150$ mg/s of argon.

3. Time-integrated, unfiltered photographs of thruster operation were brighter for thruster 20L than for thruster 38 for the same operating conditions (\dot{m} and V_0).
4. Brightness of photographs of both thrusters decreased with decreasing \dot{m} and decreasing V_C for thruster 20L (photographs were unavailable for thruster 38, but this trend would be expected in thruster 38 as well).
5. The location of brightest light appears more towards the downstream end of photographs of thruster 20L as V_C is decreased.
6. The location of brightest light appears more towards the upstream end or more towards the thruster centerline for both thrusters as \dot{m} is decreased.

7.3 Comparison of Experimental and Analytical Results

The two-dimensional performance model presented here contains assumptions regarding the formation process and physical properties of the current sheet that are likely difficult to achieve in experiments. The challenge of inductively driving high current densities in a large portion of injected propellant is exacerbated by increased propellant diffusion in thrusters employing a flat inductive coil (due in part to the lack of a cavity-like structure), though coils with a larger cone angle are predicted to outperform more cylindrical configurations in the model (owing to larger values of axial acceleration). In experiments, the thruster with a smaller cone angle demonstrated the higher performance in apparent contradiction with the conclusions drawn from results of the model. However, ideal current sheet formation (all mass immediately entrained, all mass close to the coil face, magnetically impermeable) was assumed in the model, and this assumption is likely violated in the experiment.

More tenuous current sheet formation in thruster 38 (as compared to that in thruster 20L) could be due to accelerated diffusion of propellant away from the inductive coil

caused by a wider cone angle, which would leave behind a shortage of neutral particles for ionization reactions. Also, a radial gradient in propellant density in the inductive coil could radially displace current sheet formation away from the coil face to a location where more neutral particles are available for ionization.

While the thruster with a more cylindrical coil geometry imparted the greater impulse bit to the thrust stand, the thrust measured here is significantly inferior to competing thruster designs, with displacement measurements rising barely above the noise of the data acquisition system. This decreased thrust in both thrusters studied here relative to other thruster designs is certainly attributable in part to a large inductive voltage drop in the transmission line, among other un-optimized aspects of the experimental setup as a whole. It may also be caused by premature current sheet decoupling due to radial current sheet motion or an initially radially-displaced current sheet formation point in both thrusters (one more exaggerated than the other) as described by the model. The hypothesized benefits of conical theta pinch propellant utilization appear through modeling to be counteracted by degradation in electromagnetic acceleration, suggesting that an optimal coil angle may exist. This optimal angle may increase as more sophisticated propellant injection systems are developed that are capable of maintaining more ideal density profiles in thrusters with inductive coils of various geometries.

Bibliography

- [1] Polzin, K. A. Comprehensive Review of Planar Pulsed Inductive Plasma Thruster Research and Technology. *Journal of Propulsion and Power*, 27(3):513–531, May-June 2011.
- [2] Dailey, C. L. and Lovberg, R. H. The PIT MkV Pulsed Inductive Thruster. Technical Report 191155, Lewis Research Center, Redondo Beach, CA, July 1993.
- [3] Lovberg, R. H. and Dailey, C. L. A PIT primer. Technical Report 005, RLD Associates, Encino, CA, 1994.
- [4] Polzin, K. A. Markusic, T. E. Stanojev, B. J. DeHoyos, A. and Spaun, B. Thrust Stand for Electric Propulsion Performance Evaluation. *Review of Scientific Instruments*, 77:105–108, October 2006.
- [5] Toftul, A. Wong, A. R. Polzin, K. A. and Pearson, J. B. Non-contact Thrust Stand Calibration Method for Repetitively Pulsed Electric Thrusters. *Review of Scientific Instruments*, 83, February 2012.
- [6] Burton, R. L. and Turchi, P. J. Pulsed Plasma Thruster. *Journal of Propulsion and Power*, 14(5):716–735, September-October 1998.
- [7] Polzin, K. A. Rose, M. F. and Miller, R. Operational Characteristics of a Low-Energy FARAD Thruster. Number AIAA 2008-5011, July 2008.

- [8] Dailey, C. L. and Davis, H. A. Pulsed Plasma Propulsion Technology. AFRPL-TR-73-81, TRW Systems Group, July 1973.
- [9] Josephson, V. and Hales, R. W. Parametric Study of the Conical Shock Tube. *The Physics of Fluids*, 4(3):373–379, 1961.
- [10] Josephson, V. Production of High Velocity Shocks. *Journal of Applied Physics*, 29(1):30–32, 1958.
- [11] Cruddace, R. C. and Hill, M. Mechanism of Plasma Acceleration in a Conical Theta-pinch Gun. Technical Report CLM-M52, Culham Laboratory, 1966.
- [12] Polzin, K. A. *Faraday Accelerator with Radio-frequency Assisted Discharge (FARAD)*. Ph.D. dissertation, Princeton University, Department of Mechanical and Aerospace Engineering, 2006.
- [13] Choueiri, E. Y. and Polzin, K. A. Faraday Acceleration with Radio-frequency Assisted Discharge. *Journal of Propulsion and Power*, 22(3):611–619, May-June 2006.
- [14] R. G. Jahn. *Physics of Electric Propulsion*. McGraw-Hill Book Company, 1968.
- [15] Hallock, A. K. Polzin, K. A. and Emsellem, G. D. Effect of Inductive Coil Geometry and Current Sheet Trajectory of a Conical Theta Pinch Pulsed Inductive Plasma Accelerator. Number AIAA-2011-6068, August 2011.
- [16] Hallock, A. K. Polzin, K. A. and Emsellem, G. D. Two-dimensional Analysis of Conical Pulsed Inductive Plasma Thruster Performance. Number IEPC-2011-145, September 2011.
- [17] Hallock, A. K. Polzin, K. A. . Two-dimensional Analysis of Conical Pulsed Inductive Plasma Thruster Performance. Number JANNAF-2011-2197, September 2011.

- [18] Polzin, K. A. Scaling and System Considerations in Pulsed Inductive Plasma Thrusters. *IEEE Transactions on Plasma Science*, 36(5):2189–2198, October 2008.
- [19] Eskridge, R. H. Martin, A. K. Electrical Coupling Efficiency of Inductive Plasma Accelerators. *Journal of Physics D: Applied Physics*, 38:4168–4179, December 2005.
- [20] Bernardes, J. Merryman, S. Rose, M. F. and Martin, T. H. Parameter Analysis of a Single Stage Induction Mass Driver. Technical Report PI-27, 5th IEEE Int. Pulsed Power conf., 1985.
- [21] Gooding, T. Lovberg, R. H., Hayworth, B. R. The Use of a Coaxial Gun for Plasma Propulsion. Technical Report AE62-0678, G. D. Convair, 1962.
- [22] Polzin, K. A. and Choueiri, E. Y. Performance Optimization Criteria for Pulsed Inductive Plasma Acceleration. *IEEE Transactions on Plasma Science*, 34(3):945–953, 2006.
- [23] Polzin, K. A. Reneau, J. P. and Sankaran, K. Incorporation of an Energy Equation into a Pulsed Inductive Thruster Performance Model. Number IEPC-2011-181, September 2011.
- [24] Fimognary, P. J. Cassibry, J. T. and Ims, K. E. Effects of Pre-ionization and Bias Field on Plasmoid Formation and Acceleration. Number AIAA-2007-5262, July 2007.
- [25] Eskridge, R. H. Fimognari, P. J. Martin, A. K. and Lee, M. H. Design and Construction of the PT-1 Prototype Plasmoid Thruster. Technical report, Propulsion Research Center, NASA Marshall Space Flight Center, 2005.
- [26] Niemela, C. S. and Kirtley, D. E. Initial Results on an Annular Field Reversed Configuration Plasma Translation Experiment. Technical Report AFRL-RZ-ED-TP-2008-489, Air Force Research Laboratory, November 2008.

- [27] Kirtley, D. E. Gallimore, A. D. Haas, J. and Reilly, M. High Density Magnetized Toroid Formation and Translation with xocot: An annular field reversed configuration plasma concept. Technical Report AFRL-PR-ED-TP-2007-387, Air Force Research Laboratory, August 2007.
- [28] Cubbin, E. A. Ziemer, J. K. Choueiri, E. Y. and Jahn, R. G. Pulsed thrust measurements using laser interferometry. *Review of Scientific Instruments*, 68(6):2339–2346, June 1997.
- [29] Hoskins, W. A. *Asymmetric Discharge Patterns in the MPD Thruster*. Master's thesis, Princeton University, Department of Mechanical and Aerospace Engineering, 1990.
- [30] Markusic, T. E. and Choueiri, E. Y. Photographic, Magnetic, and Interferometric Measurements of Current Sheet Canting in a Pulsed Electromagnetic Accelerator. Number AIAA 2001-3896, July 2001.
- [31] Markusic, T. E. Choueiri, E. Y. and Berkery, J. W. Measurements of Current Sheet Canting in a Pulsed Electromagnetic Accelerator. *Physics of Plasmas*, 11(10), October 2004.
- [32] Hallock, A. K. *Current Sheet Formation in a Conical Theta Pinch Faraday Accelerator with Radio Frequency Assisted Discharge*. Master's thesis, Princeton University, Department of Mechanical and Aerospace Engineering, November 2008.